

X-ray emission lines and multiphase gas in elliptical galaxies and galaxy clusters

David A. Buote^{1,3,4}, Claude R. Canizares², and A. C. Fabian¹

¹ Institute of Astronomy, Madingley Road, Cambridge CB3 0HA

² Department of Physics and Center for Space Research 37-241, Massachusetts Institute of Technology, 77 Massachusetts Avenue, Cambridge, MA 02139, U.S.A.

³ UCO/Lick Observatory, University of California at Santa Cruz, Santa Cruz, CA 95064, U.S.A.

⁴ Chandra Fellow

30 August 2018

ABSTRACT

We examine the K shell emission lines produced by isothermal and simple multiphase models of the hot gas in elliptical galaxies and galaxy clusters to determine the most effective means for constraining the width of the differential emission measure ($\xi(T)$) in these systems which we characterize by a dimensionless parameter, σ_ξ . Comparison of line ratios of two-temperature ($\sigma_\xi \ll 1$) and cooling flow ($\sigma_\xi \sim 1$) models is presented in detail. We find that a two-temperature model can approximate very accurately a cooling flow spectrum over 0.5-10 keV.

We have re-analyzed the *ASCA* spectra of three of the brightest galaxy clusters to assess the evidence for multiphase gas in their cores: M87 (Virgo), the Centaurus cluster, and the Perseus cluster. $K\alpha$ emission line blends of Si, S, Ar, Ca, and Fe are detected in each system as is significant Fe $K\beta$ emission. The Fe $K\beta/K\alpha$ ratios are consistent with optically thin plasma models and do not suggest resonance scattering in these systems. Consideration of both the ratios of H-like to He-like $K\alpha$ lines and the local continuum temperatures clearly rules out isothermal gas in each case. To obtain more detailed constraints we fitted plasma models over 1.6-9 keV where the emission is dominated by these K shell lines and by continuum. In each case the *ASCA* spectra cannot determine whether the gas emits at only two temperatures or over a continuous range of temperatures as expected for a cooling flow. The metal abundances are near solar for all of the multiphase models. We discuss the implications of these results and examine the prospects for determining the temperature structure in these systems with upcoming X-ray missions.

Key words: galaxies: general – galaxies: evolution – X-rays: galaxies.

1 INTRODUCTION

There is mounting evidence that the X-ray emission in elliptical galaxies and galaxy clusters originates from multiphase plasma. The first important evidence for multiphase gas in ellipticals and clusters came from analysis of emission lines in M87 and the Perseus cluster. Using ratios of several blends of Fe L shell lines obtained from the Focal Plane Crystal Spectrometer (FPCS) on the *Einstein* Observatory, Canizares et al. (1982) found that the hot gas in M87 emits over a large range of temperatures: from $\sim 2 - 4 \times 10^6$ K to $\sim 3 \times 10^7$ K. The strength of the Fe XVII line measured from FPCS data of the Perseus cluster also suggests a multiphase plasma (Canizares, Markert, & Donahue 1988).

Recently, data from the *ROSAT* (Trümper 1983) and

ASCA (Tanaka et al. 1994) satellites have provided new evidence for multiphase hot gas. Broad-band spectral analysis of *ASCA* data of clusters (Fukazawa et al. 1994; Fabian et al. 1994a), the brightest ellipticals (Buote & Fabian 1998; Buote 1999a), and of the brightest poor galaxy groups (Buote 1999b) indicates that the hot gas in the central regions of these systems consists of at least two temperature components. The equivalent widths and ratios of $K\alpha$ line blends of Si and S alone strongly favor multitemperature models of the *ASCA* data of the brightest ellipticals (Buote 1999a).

Complementary evidence for multiphase gas in clusters is provided by the analysis of imaging data from *ROSAT* (Trümper 1983) of cooling flow clusters which infers mass deposition rates which vary with radius approximately as $\dot{M} \propto r$ (e.g. Peres et al. 1998). This type of distributed mass

deposition is the signature of multiphase cooling flows (for a review see Fabian 1994). Multiphase cooling flows are also consistent with the positive temperature gradients observed in the centers of the brightest elliptical galaxies with *ROSAT* (e.g. Forman et al. 1993; David et al. 1994; Trinchieri et al. 1994; Rangarajan et al. 1995; Irwin & Sarazin 1996; Jones et al. 1997; Buote 1999a).

It is essential that the temperature structure be accounted for in order to deduce correctly the properties of the hot gas in these systems. The metal abundances are especially sensitive to the assumed temperature structure. For example, analyses of the X-ray spectra of elliptical galaxies where the hot gas is assumed to be isothermal always obtain very sub-solar metallicities, $Z \lesssim 0.3Z_{\odot}$, whereas when multi-temperature models are considered the metallicity of ellipticals becomes consistent with solar (see Buote & Fabian 1998 and Buote 1999a). A similar situation prevails for poor groups of galaxies (Buote 1999b).

Although this “Fe bias” is unimportant for clusters of galaxies with temperatures in excess of ~ 3 keV, if an isothermal gas is assumed for a cooling-flow cluster (or elliptical or group) then the Si/Fe and S/Fe ratios can be significantly over-estimated (see the appendix in Buote 1999b). Hence, in order to obtain reliable measurements of the heavy element abundances crucial to interpreting models of the formation, evolution, and enrichment of the hot gas in ellipticals, groups, and clusters (e.g. David, Forman, & Jones 1991; Loewenstein & Mathews 1991; Ciotti et al. 1991; Loewenstein & Mushotzky 1996; Renzini 1997; Brighenti & Mathews 1999), it is necessary to know the true temperature structure of the hot gas.

Knowledge of the temperature structure is also required to understand the contribution of discrete sources to the hard X-ray emission in elliptical galaxies. For example, if the hot gas is assumed to be isothermal then the hard spectral component measured by *ASCA* for the elliptical galaxy NGC 3923 is inconsistent with the expectation that discrete sources follow the same profile as the optical light (Buote & Canizares 1998; see also Pellegrini 1999). Finally, when multiphase cooling flows are accounted for in X-ray observations of clusters the scatter in the X-ray luminosity-temperature relationship is significantly reduced (e.g. Fabian et al. 1994b).

The Fe L shell emission lines from ~ 0.7 - 1.4 keV generally provide the strongest constraints on the temperature structure of ellipticals, groups, and clusters. There has been considerable progress in improving the accuracy of the theoretically computed Fe L shell transitions (e.g. Liedahl et al. 1995), but they are still among the most uncertain transitions implemented in the currently available plasma codes (e.g. Savin et al. 1999). There is reason for some confidence in the codes since recent empirical studies have concluded that the errors in the Fe L transitions are not overly serious (Hwang et al. 1997; Buote & Fabian 1998). (However, see the recent papers by Savin 1999 and Savin et al. 1999 for discussions of the inaccuracies in the dielectronic recombination rates used by the popular plasma codes which affect all types of emission lines.)

Nevertheless, it is important to use lines from the more-accurate K shell transitions to search for evidence of multiphase gas to complement the information from Fe L lines. To obtain the most accurate constraints on the emission

measure of a multiphase plasma it is necessary to obtain independent measurements of the temperature(s) over the entire energy range of significant emission. It is a happy coincidence that the K shell lines of many abundant elements appear throughout the X-ray wave band (0.1-10 keV).

Line ratios have important advantages over broad-band spectral fitting for probing the temperature structures of ellipticals and clusters. Firstly, in an isothermal plasma using ratios of lines of the same element avoids uncertainties in the relative abundances of the elements; there is a small dependence on metallicity in a multiphase cooling flow (section 2.2.3). Secondly, ratios of lines nearby in energy are essentially independent of Galactic or any intrinsic absorption. Thirdly, since the strength of a line can be computed using a local continuum measurement, line ratios are insensitive to any poorly constrained power-law or bremsstrahlung spectral components.

For a multiphase coronal plasma ^{*} the luminosity of an emission line arising from a transition from an upper state u to a lower state l of an element X in ionization state r may be expressed as,

$$L_{ul}(X_r) = \int \Lambda_{ul}(X_r, T) \xi(T) dT, \quad (1)$$

where $\Lambda_{ul}(X_r, T)$ is the plasma emissivity of the line at temperature T which incorporates the abundance of element X , the relative fraction of ionization state r , and other quantities depending only on the atomic physics. (The integral extends over the emitting volume V .) The quantity,

$$\xi(T) \equiv n_e^2(T) \frac{dV}{dT}, \quad (2)$$

is called the “differential emission measure” and $\xi(T) dT$ the “emission measure” at temperature T . The emission measure weights Λ as a function of temperature in equation (1) and thus effectively characterizes the temperature structure of the plasma. Notice that different phases T in general can have different electron number densities n_e .

It has been known for some time (Craig & Brown 1976) that precise constraints on $\xi(T)$ from inversion of equation (1) are difficult to obtain in practice. (For a recent discussion of this topic see, e.g., Judge, Hubeny, & Brown 1997.) That is, for a given line typically $\Lambda_{ul}(X_r, T)$ is significant over temperature ranges of factors of ~ 2 - 5 , which means that the plasma emissivity acts as a smoothing function which obscures the detailed shape of $\xi(T)$. Moreover, small uncertainties in the data are amplified by the inversion. Given these difficulties, it may only be possible to obtain relatively crude constraints on the shape of $\xi(T) dT$ for ellipticals and clusters from inversion of equation (1); e.g., width, skewness, etc [†].

The primary theoretical goal of this paper is to identify the best X-ray emission line ratios for determining the gross features of $\xi(T)$ of ellipticals and clusters with the specific objective of distinguishing between single-temperature, two-temperature, and cooling-flow spectra. (Previous dis-

^{*} The assumptions of the standard coronal model are discussed in, e.g., Sarazin (1986) and Mewe (1991).

[†] See, e.g., Kaastra et al. (1996) and Schmitt et al. (1996) for recent constraints on $\xi(T)$ of stellar coronae.

cussions of important temperature sensitive lines for clusters in the context of a different set of models may be found in Bahcall & Sarazin (1977), Sarazin & Bahcall (1977), and Canizares et al. (1982). Wise & Sarazin (1993) discuss the radial variation of the shapes of emission lines as diagnostics for cooling flow models.) To facilitate quantitative comparison of the multiphase structure of different ellipticals and clusters we introduce a quantity, σ_ξ , the “multiphase strength”. We focus on K shell emission lines since they are generally the strongest lines of ellipticals and clusters and the atomic physics is relatively simple and so the available plasma codes should be most accurate for these transitions. Because the Fe L shell lines occurring at energies $\sim 0.7 - 1.4$ keV are strong for ellipticals and clusters and are powerful as temperature diagnostics, we also examine them even though at the present time the accuracy of the plasma codes is less certain for these transitions (see above). The line ratios allow simple yet effective discrimination between popular spectral models of ellipticals and clusters and serve as an important guide to interpreting results of $\xi(T)$ obtained from inversion of equation (1).

The paper is organized as follows. In Section 2 we analyze theoretical line ratios in single-phase (Section 2.1) and multiphase (Section 2.2) models. The multiphase strength is introduced in Section 2.2.1 and it is used to elucidate the temperature structure of simple multiphase models in Section 2.2.2 and of cooling flow models in Section 2.2.3. We discuss in detail how to distinguish a two-temperature plasma from a cooling flow in Section 2.3. In Section 3 we compute and analyze line ratios of *ASCA* data of M87, the Centaurus cluster, and the Perseus cluster. Simulated observations with *Chandra*, *XMM*, and *ASTRO-E* are considered in Section 4. Finally, we comment on recent evidence for resonance scattering in 5.1 and discuss cosmological application of the multiphase strengths of clusters in Section 5.2. In Section 6 we present our conclusions.

2 THEORETICAL LINE RATIOS OF ELLIPTICALS AND CLUSTERS

We examine the theoretical emission lines predicted by coronal plasma models of ellipticals, groups, and clusters. In order to maintain a connection to feasible observations within the next 10 years, for the purposes of identifying lines we consider spectra folded through an energy resolution of 2 eV which is the targeted performance of the *Constellation-X* mission [‡]. To model the emission of a coronal plasma we use the MEKAL code which is a modification of the original MEKA code (Mewe, Gronenschild, & van den Oord 1985; Kaastra & Mewe 1993) where the Fe L shell transitions have been re-calculated (Liedahl et. al 1995). We fix the relative abundances of the elements to the (photospheric) solar values (Anders & Grevesse 1989) and, as a result, we focus on ratios of lines of the same element so that our results are not sensitive to this assumption. Finally, we do not include photo-electric absorption (Galactic or intrinsic) in this dis-

[‡] <http://constellation.gsfc.nasa.gov/>

Table 1. K Shell Transitions for H-like and He-like Ions

Isoelectronic Sequence	Transition Symbol	Transition
H	1	$1s^2 \text{S}_{\frac{1}{2}}$ — $2p^2 \text{P}_{\frac{1}{2}, \frac{3}{2}}$
	2	$1s^2 \text{S}_{\frac{1}{2}}$ — $3p^2 \text{P}_{\frac{1}{2}, \frac{3}{2}}$
	3	$1s^2 \text{S}_{\frac{1}{2}}$ — $4p^2 \text{P}_{\frac{1}{2}, \frac{3}{2}}$
	4	$1s^2 \text{S}_{\frac{1}{2}}$ — $5p^2 \text{P}_{\frac{1}{2}, \frac{3}{2}}$
He	1	$1s^2 \text{S}_0$ — $1s5p^1 \text{P}_1$
	2	$1s^2 \text{S}_0$ — $1s4p^1 \text{P}_1$
	3	$1s^2 \text{S}_0$ — $1s3p^1 \text{P}_1$
	4	$1s^2 \text{S}_0$ — $1s2p^1 \text{P}_1$
	5	$1s^2 \text{S}_0$ — $1s2p^3 \text{P}_{2,1}$
	6	$1s^2 \text{S}_0$ — $1s2s^3 \text{S}_1$

Transitions are given in the standard notation of the electron configuration (orbitals) and the level with the lower state listed first. H1 and He4-6 are all $\text{K}\alpha$ transitions while H2 and He3 are $\text{K}\beta$ transitions.

cussion[§] but include its effects when interpreting line ratios from real data (as in Section 3).

The emission lines which are perhaps the most useful for our study of the temperature structure of ellipticals and clusters ¶ are the K shell transitions involving ions of the H-like and He-like isoelectronic sequences listed in Table 1 using the standard notation (e.g. Table 3 of Mewe et al. 1985). Also very useful are the satellites to the resonance line of the preceding ion in the ionization sequence. Of particular interest are the satellite lines to the He4 resonance from dielectronic recombination to autoionizing states of the Li-like ion. The strongest of these satellite lines typically come from the multiplet $1s^2 2p^2 \text{P} - 1s2p^2 \text{D}$. Finally, the L shell transitions of Fe between $\sim 0.7 - 1.4$ keV (especially the 2s-3p lines) are strong and very temperature sensitive, though most are unresolved at 2 eV resolution and thus blends of lines are emphasized below.

We identified significant K and Fe L shell lines between 0.4 - 10 keV from visual inspection of isothermal MEKAL models. These models were viewed at 2 eV resolution and had temperatures ranging from 0.1 - 10 keV||. We restricted our attention to this energy range because below ~ 0.4 keV Galactic photo-electric absorption is prohibitive, and energies above ~ 10 keV will not be effectively probed by high energy resolution X-ray satellites expected to operate in the near future.

For lines that are not isolated at the 2 eV resolution, our chosen energy boundaries in many cases enclose other emission lines from the same element or others. The result is that the line ratios we discuss below often behave differently over some temperature ranges than expected if there were no blending of lines. However, we enforce that such peculiarities are not the result of uncertainties in defining the continuum because the line luminosities are computed from the models using a finer energy resolution which allows the

[§] We discuss the possible complication of resonance scattering in Section 5.1.

¶ A summary of standard temperature diagnostics of coronal plasmas may be found in Mewe (1991).

|| Throughout the paper we quote temperatures in units of keV ($k_B T$).

Table 2. Energy Ranges of Satellite Lines

Ion(s)	Energy Range (keV)	Isoelectronic Sequence
Si XII	1.847-1.852	Li
S XIV	2.436-2.445	Li
Ar XVI	3.130-3.137	Li
Ca XVII/XVIII	3.863-3.875	Be/Li blend
Fe XX/XXI	6.610-6.630	N/C blend (sat1)
Fe XVIII/XIX	6.520-6.610	F/O blend (sat2)
Ni XXV	7.725-7.747	Li

Energy ranges used to define the dielectronic recombination satellite lines.

continuum to be accurately subtracted. Within the energy boundaries used to define a line (or blend) we compute the total emission above the continuum on an energy grid of 15000 logarithmically spaced energy bins over 0.4 - 10 keV; i.e. ~ 0.2 eV bins around 1 keV and ~ 1.5 eV bins around 7 keV.

Our procedure to define the continuum for the lines of interest begins by identifying from visual examination of the spectrum a nearby bin at lower energy having no apparent lines. This choice is made after examining spectra of several temperatures. (Note that we avoid energy bins having strong recombination edges.) Let us denote the continuum emission at this energy bin, $j_c(E_i)$, where E_i is the energy of this bin i . Proceeding to the next bin ($i+1$) with energy E_{i+1} , if there is no line emission in this bin, then the total emission $j(E_{i+1})$ is all continuum such that $j(E_{i+1}) \leq j_c(E_i)$ since (at a fixed temperature) the (free-free) continuum is a monotonically decreasing function of energy. In this case, $j_c(E_{i+1}) \equiv j(E_{i+1})$ becomes our new definition of the continuum. If there is line emission in bin $i+1$ so that $j(E_{i+1}) > j_c(E_i)$, then we set $j_c(E_{i+1}) \equiv j_c(E_i)$. This procedure is followed up to and through the lower boundary of the emission line of interest until the upper boundary of the line region is reached. The continuum values ($j_c(E_i), j_c(E_{i+1}), \dots$) are subtracted from the corresponding bins of the line region.

2.1 Isothermal case

We begin by examining isothermal plasma models in detail since the temperature dependences of line strengths and line ratios are most easily understood for these models. We plot spectral regions in Figure 1 corresponding to the strongest K shell transitions of Si, S, Ar, and Fe. In Figure 2 we plot the luminosities of the K shell emission lines of Si XII-XIV and Fe XXIII-XXVI obtained from the isothermal models; these ions have among the strongest K shell lines which are also isolated from strong lines of other elements. Since the Li-like satellites of Fe XXIV are unresolved at 2 eV resolution, the Fe satellites plotted in Figure 2 result from ions in the next few isoelectronic sequences. In Table 2 we list the energy ranges used to define these satellite blends for Fe as well as the Li-like satellites of the other elements.

In Figure 3 we plot as a function of temperature the ratios of the K shell emission lines of the abundant elements. (Ratios involving lines that are very contaminated are not plotted.) The ratios of lines emitted from subsequent ionization stages of the same element (H1/He4, Satellite/He4)

are overall more useful as temperature diagnostics than are the ratios involving lines of the same ion (H2/H1, He3/He4). The former, however, rely on the assumption of ionization equilibrium which can be checked using the latter ratios. Ionization equilibrium is expected to be an accurate approximation for the hot gas in ellipticals, groups, and clusters, even those with cooling flows (Canizares et al. 1988).

The H1/He4 ratio is probably the most useful because the H1 and He4 transitions give rise to the strongest lines and the ratio ~ 1 where the lines have maximum luminosity; see the examples of Si and Fe in Figure 2. The mostly smooth curves of the H1/He4 ratios as a function of temperature in Figure 3 demonstrate that the H1 and He4 lines of many of the abundant elements can be measured accurately at 2 eV resolution. The largest distortions are evident for the Mg ratio which result from contamination in the measurement of the Mg XI He4 transition by Fe L emission. Other significant contamination appears in the computation of the Fe XXV He4 transition which includes unresolved Li satellites at 2 eV resolution.

Since the H1/He4 ratios for the different elements take a value of 1 approximately uniformly distributed over the logarithmic range of temperatures ~ 0.5 - 10 keV, accurate estimation of any temperature over this range can be obtained by H1/He4 ratios of more than one element. For temperatures below ~ 0.5 keV the only useful H1/He4 ratio is that of oxygen.

The next most useful diagnostic is the Satellite/He4 ratio, where “Satellite” typically refers to the Li-like satellites; see Table 2 for the definitions of the satellite lines used. The principal difficulty here is measuring the satellite lines because they are usually much weaker than the He4 line and are difficult to resolve from the (forbidden) He5 line, especially for elements with atomic number $\lesssim 20$. The shapes of the temperature profiles of the Satellite/He4 ratios of Si, S, Ca, and Ni are similar in Figure 3. The ratio of Fe K lines has a steeper profile because satellites from isoelectronic sequences above Li are used; i.e. sat1 in Table 2. The distorted temperature profile of the Ar ratio for $T \lesssim 1$ keV arises from unresolved Li satellites being included in the He4 line.

Over $T \sim 0.5$ - 5 keV the Si Satellite/He4 ratio changes by a factor ~ 20 compared to ~ 1000 for the Si H1/He4 ratio. The steepest Satellite/He4 profile shown is for Fe K. Even if we do not consider $T < 2$ keV where the Fe K lines are weak, then the Satellite/He4 ratio changes by a factor of ~ 50 from $T \sim 2$ - 8 keV. This variation is about as large as seen for the Fe K H1/He4 ratio.

The H2/H1 (i.e. Ly β /Ly α) ratios are much less temperature sensitive than are the ratios described previously. The temperature dependence of this ratio is simply, $H2/H1 \propto \exp[-(E2 - E1)/k_B T]$, where k_B is Boltzmann’s constant and $E2$ and $E1$ are the energies of the H2 and H1 lines respectively. For Si, $E2 - E1 = 0.37$ keV, and as is clear from Figure 3, H2/H1 only varies significantly for temperatures within approximately a factor of 2 of 0.37 keV. At these temperatures the hydrogenic lines of Si are also very weak. This behavior holds qualitatively for the other elements shown. (Note that the plotted S ratio is actually H3/H1 because the H2 transition is blended with the Ar XVIII He6 intercombination line.) Typically, for temperatures where the lines are at their strongest, the H2/H1 ratio varies by at most a factor of 2; e.g. Si from 0.5-5 keV.

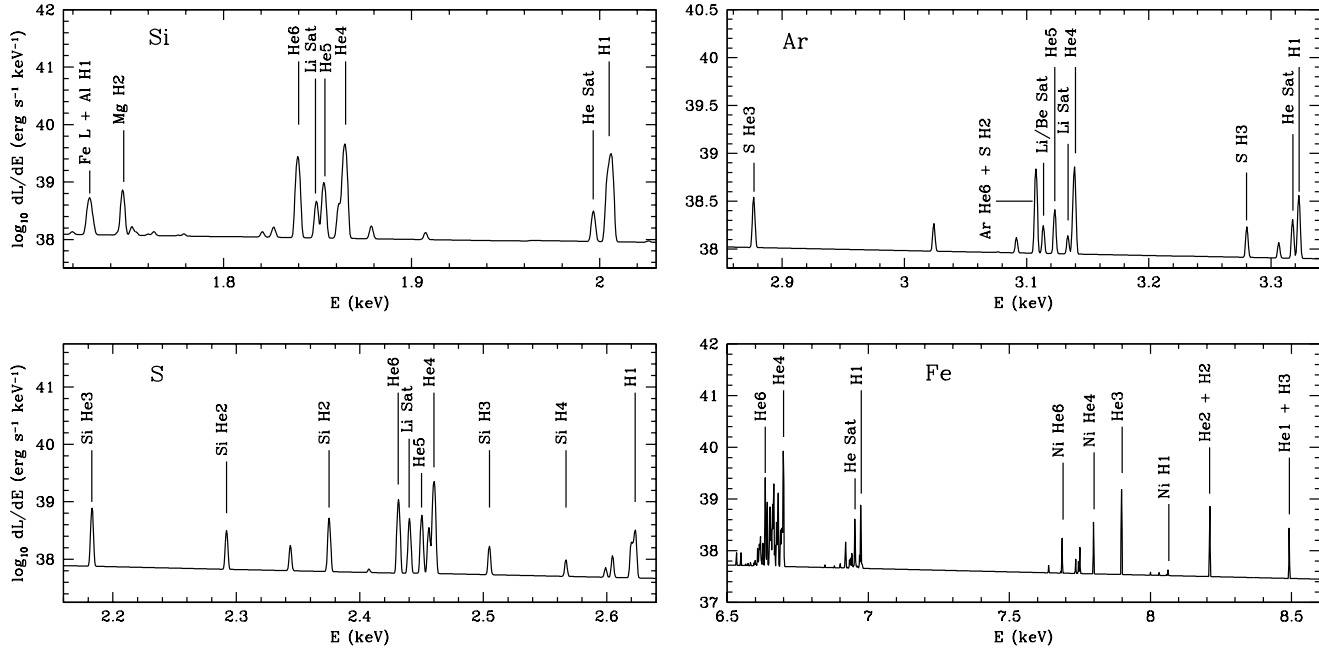


Figure 1. Each panel shows a portion of the X-ray spectrum where the K shell emission lines are prominent for an important abundant element: Si XII-XIV, S XIV-XVI, Ar XVII-XVIII, and (mainly) Fe XXV-XXVI. The spectra are computed for isothermal MEKAL models with $Z = 0.5Z_{\odot}$ and are plotted at 2 eV energy resolution; the temperatures are 1 keV for the Si and S panels, 2 keV for Ar, and 4 keV for Fe. The transitions mentioned in the text are labeled in each figure according to the notation in Table 1; the labels include the name of the element only if it is not the element labeled on the panel. The luminosity is calculated for a total emission measure $n_e^2 V = 10^{65} \text{ cm}^{-3}$ appropriate for M87 (e.g. Canizares et al. 1982) which is approximately midway between the luminosities of ellipticals and clusters.

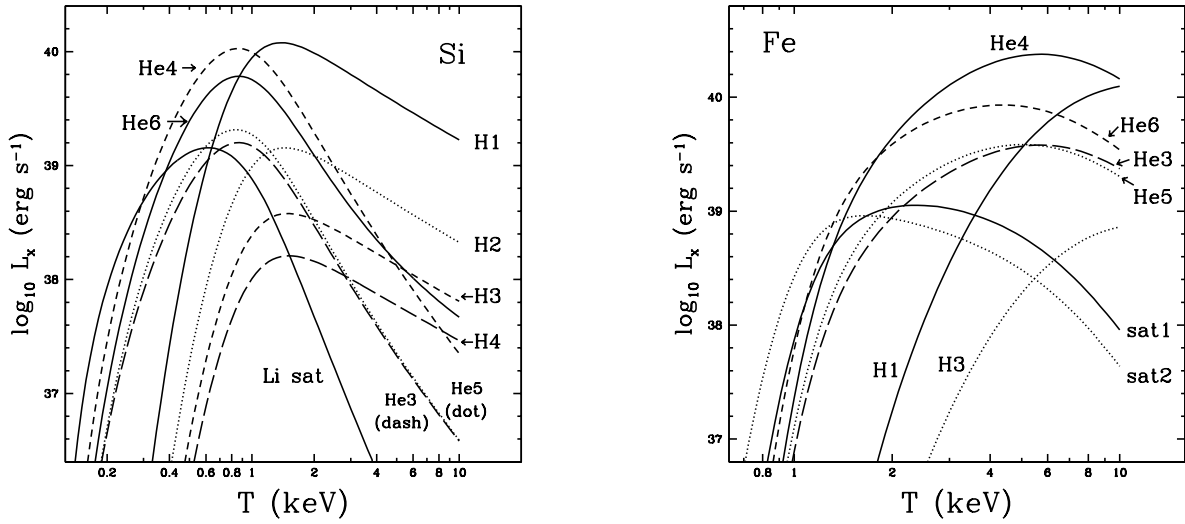


Figure 2. Emission lines of K shell transitions of Si XII-XIV (left) and Fe XXIII-XVI (right) computed in isothermal MEKAL models with $Z = 0.5Z_{\odot}$ and $n_e^2 V = 10^{65} \text{ cm}^{-3}$ as in Figure 1. See text in Sections 2 and 2.1 for details regarding the definitions of these lines.

Similar to H₂/H₁, the ratio He₃/He₄ (i.e. K β /K α) involves lines of the same isoelectronic sequence and has a fairly weak temperature dependence for temperatures where the lines are of significant strength. Taking S for an example (Figure 3), for temperatures ranging from 0.5 - 5 keV the He₃/He₄ ratio varies by only ~ 5 - 10 per cent. For $T \lesssim 0.5$

keV, the ratio is very sensitive to temperature, but the lines are also very weak: at $T = 0.25$ keV we have $\log_{10} L_x = 36.1$ and 36.7 for He₃ and He₄ of S assuming a total emission measure of 10^{65} cm^{-3} (as in Figure 2). Probably Fe XXV is the most useful ion for this ratio because at ~ 2 keV where He₃/He₄ begins to change noticeably, the emission

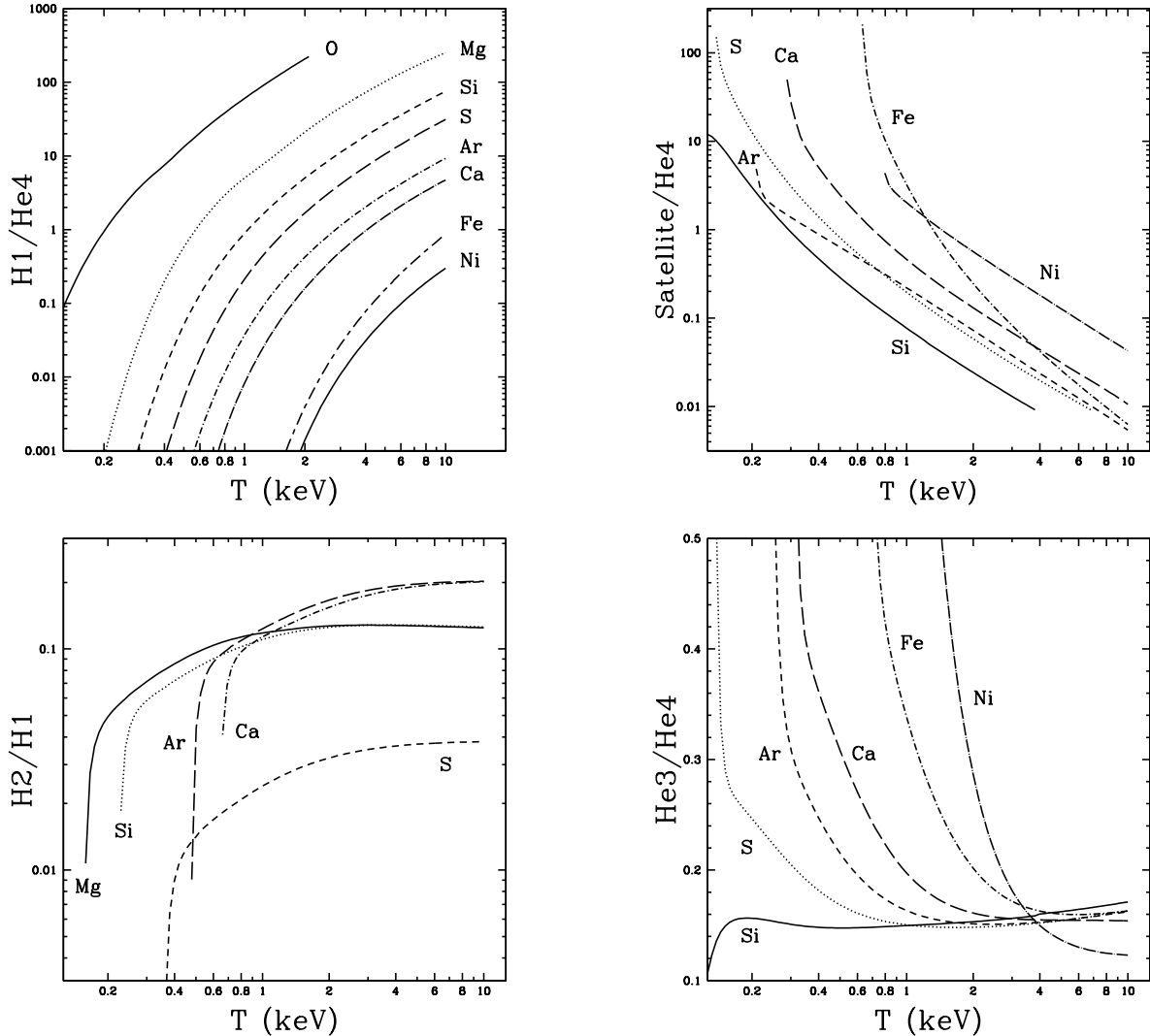


Figure 3. Emission line ratios of K shell transitions (Tables 1 and 2) of abundant ions in isothermal MEKAL models. Note the linear scale for He3/He4.

lines still have significant emissivity; e.g., at $T = 2$ keV we have $\log_{10} L_x = 39.0$ and 39.6 for He3 and He4 of Fe (see Figure 2). Hence, for Fe the He3/He4 ratio varies by about a factor of 10 over interesting temperatures. (Note that the Si ratio turns over below 0.2 keV because of weak Al XI contamination in the He4 line of Si XIII.)

For any individual element, the ratios described above involve lines which differ in energy by < 1 keV. That is, each ratio gives a measure of the temperature in a small energy region of the spectrum. Comparing these ratios for different elements over the entire X-ray spectrum allows one to examine the consistency of the temperatures measured by each ratio. Another method to compare lines that are substantially different in energy is to compare ratios of lines of the same isoelectronic sequences of different elements (Figure 4). Although these ratios depend on the relative abundances of the elements, they can provide an interesting consistency check of the other ratios. (In fact, these ratios are used to measure abundances once $\xi(T)$ is known.) Typically, these ratios vary by a factor of 100 over the temperature ranges where the lines emit significantly (Figure 4). (These ratios

have a stronger dependence on N_H since the lines are not close together in energy, but for energies above ~ 2 keV the dependence should be negligible.)

Finally, we consider the Fe L shell emission lines. Even at 2 eV resolution most of the Fe L lines between 0.7-1.4 keV are not resolved. From visual inspection of the MEKAL model spectra we identified blends of nearby lines which varied similarly with temperature and were least contaminated by lines of other elements. In Table 3 we list energy ranges for five blends (or, more accurately, groups) of lines and plot their strengths and ratios as a function of temperature in Figure 5. These line groups of $\sim 10 - 20$ eV width are shown because they have the most regular behavior over the temperature range investigated. (The lack of blends between 1.1-1.3 keV is due to the difficulty of finding groups uncontaminated by emission lines of other elements.) It is clear from comparison to the K shell strengths and ratios discussed previously that the Fe L lines are very strong and very temperature sensitive over energies $\sim 0.2 - 5$ keV; e.g. the 2:1 ratio varies by a factor of ~ 1000 over 0.2 - 1.5 keV. The superior performance of the Fe L line ratios highlights

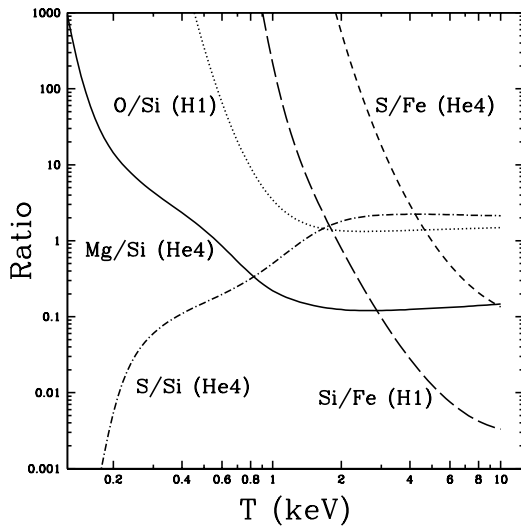


Figure 4. Ratios of K shell emission lines from the same isoelectronic sequences of different elements for isothermal MEKAL models with $Z = 0.5Z_{\odot}$.

Table 3. Energy Ranges of Fe L Blends

Blend	Energy Range (keV)	Dominant Ion(s)
1	0.722-0.741	Fe XVII
2	0.867-0.878	Fe XVII & XVIII
3	0.940-0.975	Fe XVII & XVIII
4	1.375-1.387	Fe XXII
5	1.435-1.445	Fe XXIII

the importance of improving the accuracy of the plasma codes for these transitions. It may be that future observations will shed light on the accuracy of the codes in the Fe L region by comparing to the temperatures inferred from K shell transitions.

2.2 Multiphase cases

We now examine the ability of the line ratios to quantify the general multiphase structure of the hot gas in ellipticals, groups, and clusters. The temperature structure is fully characterized by the distribution of emission measure as a function of temperature (see Introduction). Of particular relevance to ellipticals, groups, and clusters are emission measures of a single temperature component, a cooling flow component (see below), or a mixture of both. The single temperature component is often modeled as a δ -function differential emission measure while a multiphase cooling flow emits over a wide range of temperatures. Hence, to facilitate our discussion of the temperature structures of ellipticals and clusters, we wish to define a dimensionless parameter, σ_{ξ} , which isolates the information contained in $\xi(T)$ indicating the multiphase “width” or “strength”. (We discuss a possible cosmological application of σ_{ξ} in Section 5.2.)

2.2.1 Multiphase strength

We first consider the case where $\xi(T)$ does not contain any δ -function components. This is the physical situation since in a real elliptical or cluster the hot gas will always have some temperature fluctuations about the mean as a result of incomplete relaxation.

Over some temperature range (T_{\min}, T_{\max}) it is necessary to define the “maximal multiphase strength” which we take to be $\xi(T) = \text{constant}$; i.e. for T within this range the emission measure, $\xi(T)dT$, is constant for fixed intervals dT . For constant ξ the total emission measure equals $\xi\Delta T$, where $\Delta T = T_{\max} - T_{\min}$. If $\xi(T)$ is centrally peaked (i.e. approximately a single phase) then $\xi_{\max}\Delta T$ will greatly exceed the total integrated emission measure. Thus, a sensible definition for the “multiphase strength” of an emission measure distribution is,

$$\sigma_{\xi} \equiv \left(\frac{\int_{T_{\min}}^{T_{\max}} \xi(T) dT}{\xi_{\max}\Delta T} \right) \frac{\Delta T}{2\langle T \rangle} \quad (3)$$

$$= \frac{1}{2\langle T \rangle \xi_{\max}} \int_{T_{\min}}^{T_{\max}} \xi(T) dT, \quad (4)$$

where ξ_{\max} is the maximum value of ξ , $\langle T \rangle$ is the emission measure weighted temperature,

$$\langle T \rangle = \frac{\int_{T_{\min}}^{T_{\max}} T \xi(T) dT}{\int_{T_{\min}}^{T_{\max}} \xi(T) dT}, \quad (5)$$

and (T_{\min}, T_{\max}) are any two temperatures which bracket the region in temperature space where $\xi \neq 0$. The factor $\Delta T/2\langle T \rangle$ in equation (3) takes into account the size of the temperature interval; i.e. for uniform ξ we have $\sigma_{\xi} = \Delta T/2\langle T \rangle \ll 1$ for a narrow interval $T_{\max} \approx T_{\min}$ (i.e. approximately single phase) but $\sigma_{\xi} = \Delta T/2\langle T \rangle \sim 1$ for $T_{\max} \gg T_{\min}$. Thus, σ_{ξ} is a measure of the fractional width of ξ .

To illustrate the meaning of σ_{ξ} let us for the moment consider ξ to be a Gaussian with standard deviation σ and mean temperature $\langle T \rangle$. In this case there is an analytic expression for the multiphase strength,

$$\sigma_{\xi} = \sqrt{\frac{\pi}{2}} \frac{\sigma}{\langle T \rangle} \quad (\text{Gaussian}), \quad (6)$$

which implicitly assumes $(T_{\min}, T_{\max}) = (-\infty, +\infty)$ but is accurate provided $\Delta T \gg \sigma$. As would be expected, $\sigma_{\xi} \propto \sigma$, indicating that σ_{ξ} measures the width of the emission measure distribution, but σ_{ξ} applies equally well to ellipticals and clusters because the mean temperature, $\langle T \rangle$, is divided out.

The definition of multiphase strength just described is applicable for all “well behaved” $\xi(T)$. However, it is often convenient to fit models consisting of individual δ -function temperature components to X-ray data of ellipticals and clusters. This widespread practice is well justified for nearly isothermal systems because the true finite width of $\xi(T)$ cannot be distinguished from a δ -function due to the limitations in the energy resolution of current X-ray data. Hence, since δ -function temperature components (even though they are not quite physical) are often fitted to data of ellipticals, groups, and clusters, we consider how to modify the definition of σ_{ξ} so that it applies for emission measure distri-

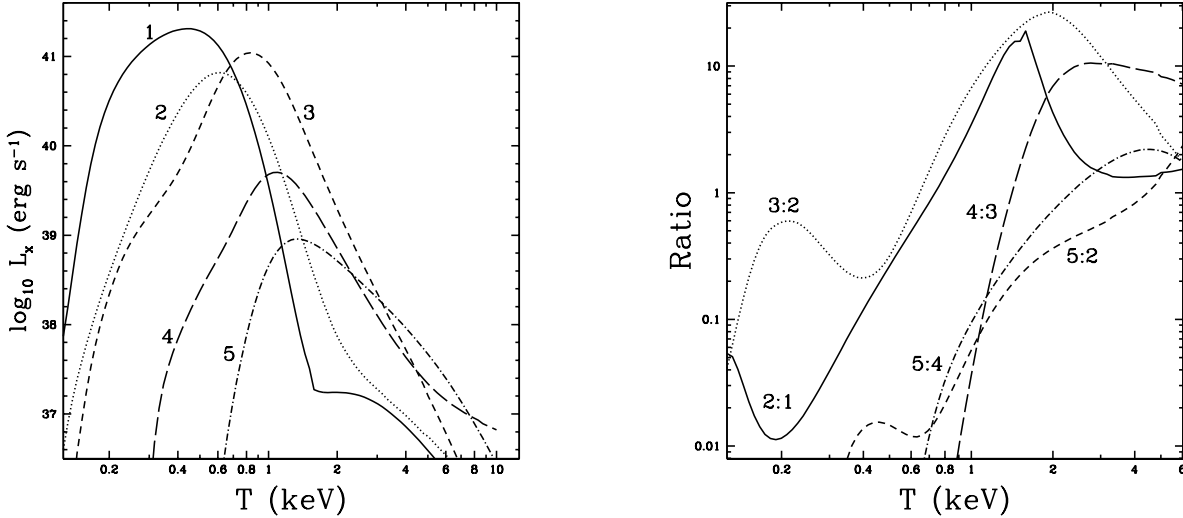


Figure 5. Fe L emission line strengths (left) and ratios (right) computed in isothermal MEKAL models with $Z = 0.5Z_{\odot}$. The lines correspond to the definitions in Table 3. The luminosity is calculated for a total emission measure $n_e^2 V = 10^{65} \text{ cm}^{-3}$ as in Figure 1.

butions having only δ -function temperature components or having both a δ -function and “well behaved” temperature components.

For $\xi(T)$ consisting of a single δ -function temperature component we have $\sigma_{\xi} = 0$ because $\xi_{\max} = \infty$. This indicates correctly that the width of the emission measure distribution is zero. However, if we consider $\xi(T)$ to be composed of a single δ -function component plus some “well behaved” component such as a Gaussian, then σ_{ξ} is still zero regardless of the shape of the “well behaved” component. When considering emission measure distributions composed of both a δ -function temperature component and other non-singular components, it is reasonable to modify σ_{ξ} according to the fractional contribution of the “well behaved” component to the total integrated emission measure. That is, if EM_{ns} and EM_{δ} are the total emission measures of the non-singular and δ -function components respectively, then the total multiphase strength is constructed by replacing σ_{ξ} of the non-singular component by $f\sigma_{\xi}$, where $f = \text{EM}_{\text{ns}}/(\text{EM}_{\text{ns}} + \text{EM}_{\delta})$. This form of the multiphase strength is especially useful when considering models consisting of a mixture of a cooling flow and ambient gas (as in Sections 2.2.3, 2.3, and 5.2).

The definition of σ_{ξ} cannot be so easily modified if $\xi(T)$ consists of multiple δ -functions. A differential emission measure consisting of a finite sum of N δ -function temperatures, $\xi(T) = \sum_{i=1}^N \xi_i \delta(T - T_i)$, always has $\sigma_{\xi} = 0$ independent of the ξ_i and N . Clearly σ_{ξ} should depend on N and on the temperature difference between each δ -function. To simplify let us restrict ourselves to the case where the δ -functions are evenly spaced in temperature. In the limit of large N we can generalize σ_{ξ} to the discrete case σ_{ξ}^N by simply replacing $\xi_{\max} \Delta T$ in equation (3) with $N \xi_{\max}$. This is appropriate for $N \gg N_c$, where N_c is some critical number of δ -functions above which a discrete number of phases is a good approximation to a continuous $\xi(T)$. In the other limit we require that $\sigma_{\xi}^N \rightarrow 0$ as $N \rightarrow 1$. Considering these limits we define σ_{ξ}^N as follows,

$$\sigma_{\xi}^N \equiv \left(\frac{\sum_{i=1}^N \xi_i}{N \xi_{\max}} \right) \frac{\Delta T}{2\langle T \rangle} \left(1 - e^{-(N-1)/N_c} \right). \quad (7)$$

The first two terms are just the straightforward generalization of σ_{ξ} for large N while the last term is an arbitrary means to smoothly connect the limiting cases. A reasonable choice for N_c is ~ 20 .

2.2.2 Simple examples

We plot the H1/He4 ratio of Si as a function of temperature in Figure 6 for MEKAL models consisting of two temperatures with equal emission measures. For clarity we express σ_{ξ}^N as the product of two factors: (1) the terms which are the generalization of σ_{ξ} for large N , and (2) the factor involving the number of temperature components which is 0.05 for $N = 2$ and $N_c = 20$. Even for relatively small $\sigma_{\xi}^N = 0.25 \times 0.05$ there are considerable departures from the isothermal case. Of particular interest is that there are values of $\langle T \rangle$ where very different σ_{ξ}^N have very similar line ratios. Just above 1 keV the ratios for models with $\sigma_{\xi}^N = 0$ and 0.5×0.05 differ by only ~ 15 per cent. Just below $\langle T \rangle = 3$ keV the curves of $\sigma_{\xi}^N = 0$ and 0.9×0.05 intersect!

The key implication of these curves is that one line ratio does not uniquely determine σ_{ξ}^N . The situation is even more complicated than shown in Figure 6 if the two temperature components are allowed to have different emission measures. In that case models having the same $\langle T \rangle$ and σ_{ξ}^N can also have different line ratios. These degeneracies are related to the ambiguity in determining $\xi(T)$ from inversion of equation (2) (see Introduction). To narrow the region of σ_{ξ}^N space, one must add constraints from similar ratios of other elements and use as many temperature sensitive ratios as possible (e.g. satellite/He4).

The situation is more tractable for a simple non-singular differential emission measure such as a constant or a Gaussian. In Figure 6 we show the Si H1/He4 ratio versus temperature for the case $\xi = \text{constant}$. The ratio profile changes slowly away from the isothermal curve and flattens for larger

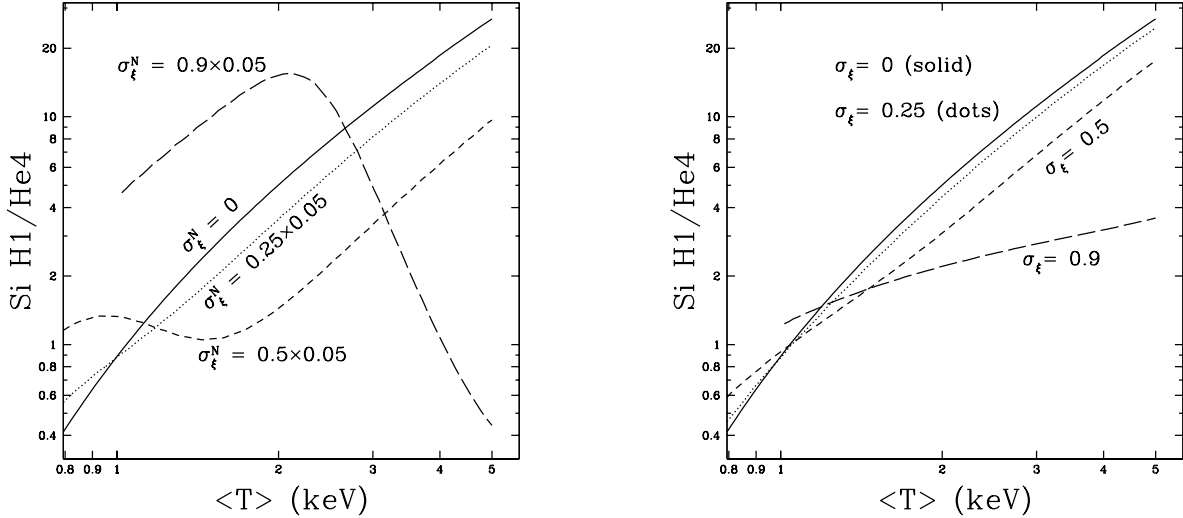


Figure 6. H1/He4 ratio for Si versus emission measure weighted temperature for two-temperature models, $\xi(T) \propto \delta(T - T_1) + \delta(T - T_2)$ (left), and models with a constant differential emission measure, $\xi = \text{constant}$, over some temperature range (right). Each curve corresponds to a different multiphase strength. For the constant ξ case (right) the multiphase strength is given by σ_ξ (equation 4) and for (left) the δ -function case σ_ξ^N (equation 7) for $N = 2$ and $N_c = 20$.

σ_ξ which is just $\Delta T / 2\langle T \rangle$ for a constant ξ . Again, for the Si ratio there is a $\langle T \rangle$ near 1 keV where a large range of σ_ξ have nearly the same H1/He4 ratio; i.e. even for this rigid model, more than one line ratio is required to constrain σ_ξ . Notice, however, that there are large regions of ratio- $\langle T \rangle$ space which are uninhabited. In particular, the accessible region of the $\xi = \text{constant}$ model ends not much below the line $\sigma_\xi = 0.9$. This also applies for any continuous $\xi(T)$ since $\xi = \text{constant}$ is defined to be the limiting case for maximal multiphase strength. (Note that a Gaussian model has behavior similar to that of the constant ξ in Figure 6.)

From examination of plots like Figure 6 for different elements we can locate the critical value of σ_ξ that represents the boundary between approximately single-phase and strongly multiphase ξ . If we define ξ to be significantly multiphase when the H1/He4 line ratios of Si (and others) typically differ by more than 10 per cent from the isothermal case, then $\sigma_\xi \sim 0.2$ represents the boundary between approximately single-phase and significantly multiphase ξ . This criteria applies for a constant and Gaussian ξ . When a δ -function is added to these models we find that $\sigma_\xi \sim 0.1$ is a better representation of the transition between a single-phase and multiphase gas.

2.2.3 Cooling flows

A physical mechanism for producing multiphase gas in ellipticals, groups, and clusters is provided by cooling flows (Fabian, Nulsen, & Canizares 1984; Nulsen 1986, 1997; Thomas, Fabian, & Nulsen 1987; White & Sarazin 1987; for a recent review see Fabian 1994). In these models gas cools out of the flow in regions where the cooling time is sufficiently short (usually taken to be less than the assumed age of the system). The simplest example is for gas cooling at constant pressure from some upper temperature T_{\max} in which case the conservation of enthalpy implies an energy release dL within a temperature interval dT of,

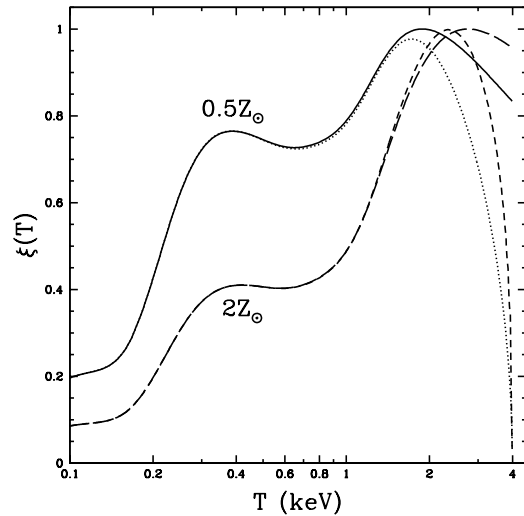


Figure 7. The differential emission measures for a constant pressure cooling flow ($Z = 0.5Z_\odot$ – solid, $Z = 2Z_\odot$ – long dash) and for a cooling flow with $\dot{M} \propto r$ in the gravitational potential of a singular isothermal sphere ($Z = 0.5Z_\odot$ – dotted, $Z = 2Z_\odot$ – short dash). All models have $T_{\max} = 4$ keV. The units of ξ (for each metallicity) are normalized to the maximum value of ξ for the constant pressure cooling flow.

$dL = 5\dot{M}k_BdT/2\mu m_p$, where μ is the mean atomic weight, m_p the proton mass, and \dot{M} is the rate of mass deposition. Comparing this expression to equation (1) one obtains the differential emission measure,

$$\xi(T) = \frac{5}{2} \frac{\dot{M}k_B}{\mu m_p} \frac{1}{\Lambda(T)} \quad (\text{Constant Pressure CF}), \quad (8)$$

for $T \leq T_{\max}$ which we plot in Figure 7 for $T_{\max} = 4$ keV with abundances $Z = 0.5, 2Z_\odot$. The shape of $\xi(T)$ is sensitive to Z , particularly for $T \lesssim 1$ keV where the Fe L shell

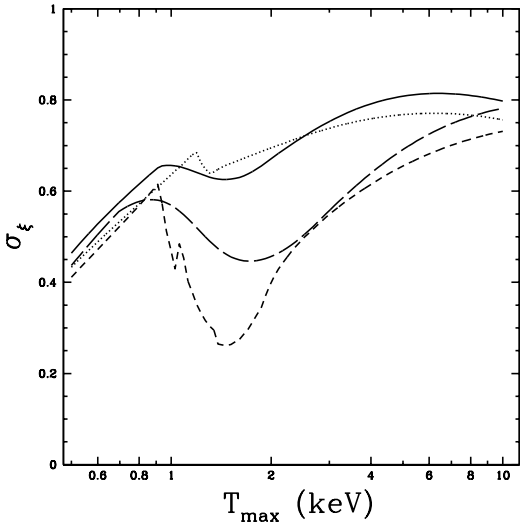


Figure 8. Multiphase strengths for the cooling flow models in Figure 7. See text for discussion of the behavior near 1 keV.

lines dominate $\Lambda(T)$. However, since most of the emission measure, $\int \xi(T) dT$, in the models in Figure 7 result from temperatures between ~ 2 - 4 keV, these metallicity differences do not translate to large differences in the K shell line ratios as we show below.

The emission measure weighted temperatures for the models with $Z = 0.5Z_{\odot}$ range from $\langle T \rangle \approx 0.6T_{\max}$ for $T_{\max} = 0.5$ keV to $\langle T \rangle \approx 0.5T_{\max}$ for $T_{\max} = 10$ keV. The luminosity weighted temperatures are ≈ 15 per cent larger than $\langle T \rangle$. For $Z = 2Z_{\odot}$, $\langle T \rangle$ ranges from $\langle T \rangle \approx 0.4T_{\max}$ for $T_{\max} = 0.5$ keV to $\langle T \rangle \approx 0.8T_{\max}$ for $T_{\max} = 10$ keV.

The multiphase strength as a function of T_{\max} is shown in Figure 8. Over $T_{\max} = 0.5$ - 10 keV we have $\sigma_{\xi} \sim 0.45$ - 0.8 for both $Z = 0.5Z_{\odot}$ and $Z = 2Z_{\odot}$ and thus the constant pressure cooling flow has nearly maximal multiphase strength for the temperatures of ellipticals, groups, and clusters. The $Z = 2Z_{\odot}$ case lies below the $Z = 0.5Z_{\odot}$ model but they approach each other at the largest values of T_{\max} . Note that the wiggles in σ_{ξ} are simply due to the same wiggles in Λ .

In Figure 9 we show the H1/He4 line ratios of the constant pressure cooling flow (with $Z = 0.5Z_{\odot}$) as a function of T_{\max} . The H1/He4 profiles are markedly different from the single temperature case shown in Figure 3. The differences are most striking for those lines with $E \lesssim 2$ keV. In particular, the O H1/He4 profile changes by only a factor of ~ 3 while the single temperature profile changes by several orders of magnitude over the temperature range shown. (The O lines are much stronger in the cooling flow models as well.) In addition to the K shell lines, the Fe L line ratios (not shown) also have very different profiles from the isothermal case making them very powerful for constraining the properties of cooling flows (e.g. Canizares et al. 1982, 1988).

The line ratios are very similar for the $Z = 2Z_{\odot}$ case where the Ca and Fe H1/He4 profiles deviate from those in Figure 9 by less than ~ 5 per cent over the whole temperature range plotted. The O and Si ratios show larger deviations which increase with increasing T_{\max} ; i.e. above 2

keV the O and Si ratios are larger by ~ 20 - 40 per cent and ~ 10 - 20 per cent respectively for the $Z = 2Z_{\odot}$ case.

Since only regions where the cooling time is less than the age of the system participate in the cooling flow, the observed X-ray flux will generally include emission from the non-cooling “ambient” phase. In Figure 9 over the constant pressure model we also plot the H1/He4 ratios of a model consisting of a constant pressure cooling flow of temperature, T_{\max} and a single temperature model with temperature, $T = T_{\max}$ where the cooling-flow and isothermal components have equal total emission measure. The line ratio profiles of the composite models have reasonably similar shapes to the case of the cooling flow alone, but they are shifted up by ~ 10 - 40 per cent. The largest differences occur at the largest temperatures for the lines with the highest energies.

The reason why the composite model still has line ratios markedly different from the isothermal case is that each component has the same total emission measure which implies $f = 0.5$ and $\sigma_{\xi} \rightarrow 0.5\sigma_{\xi}$ for the composite cooling flow and δ -function model (see section 2.2.1); i.e. the values of σ_{ξ} range from ~ 0.3 - 0.4 . As noted at the end of the previous section, the boundary between approximately single-phase and significantly multiphase emission measure distributions occurs for $\sigma_{\xi} \sim 0.1$ when ξ includes a δ -function component. Thus, a model with a cooling flow component and a single-phase component has line ratios similar to an isothermal gas for $f \lesssim 1/7$ and $\text{EM}_{\delta}/\text{EM}_{\text{cf}} \gtrsim 6$. (Note this applies for $Z = 0.5Z_{\odot}$ but is similar for $Z = 2Z_{\odot}$ where we deduce $f \lesssim 1/5$ and $\text{EM}_{\delta}/\text{EM}_{\text{cf}} \gtrsim 4$.)

It is worth considering how much these properties change for a more sophisticated multiphase cooling flow model that allows for gravitational work to be done on the flow as it cools. Nulsen (1998) has derived $\xi(T)$ for a cooling flow in the gravitational potential of a singular isothermal sphere. For $T \ll T_{\max}$ the differential emission measure of this isothermal sphere cooling flow model is equivalent to the constant pressure case (equation 8). In contrast, $\xi(T_{\max}) = 0$ for the isothermal sphere cooling flow. The detailed shape for intermediate temperatures depends on the slope η of the mass deposition profile, $\dot{M} \propto r^{\eta}$.

We plot $\xi(T)$ and σ_{ξ} for $\eta = 1$ in Figures 7 and 8 for comparison to the constant pressure case. Except for $T_{\max} \sim 1$ - 2 keV, the multiphase strength for the $Z = 0.5Z_{\odot}$ case is slightly smaller for the isothermal sphere cooling flow; the differences are more drastic for the $Z = 2Z_{\odot}$ case. The emission measure weighted temperatures for these models are ~ 5 - 10 per cent smaller than those of the constant pressure cooling flow.

There is an abrupt change in σ_{ξ} near 1 keV for the isothermal sphere cooling flow models. Let us focus on the $Z = 0.5Z_{\odot}$ case first. Near 1.2 keV ξ_{\max} jumps from its location near the local maximum at 0.36 keV to a temperature just below T_{\max} (see Figure 7). As T_{\max} increases over the next ~ 0.3 keV we have ξ_{\max} increasing faster than the total emission measure translating to a decrease in σ_{ξ} . This change is much more abrupt for the isothermal sphere cooling flow because of the enforced condition that $\xi(T_{\max}) = 0$. This overall behavior is more pronounced for the $Z = 2Z_{\odot}$ case because of the details of the strong Fe L shell lines are proportionally more important.

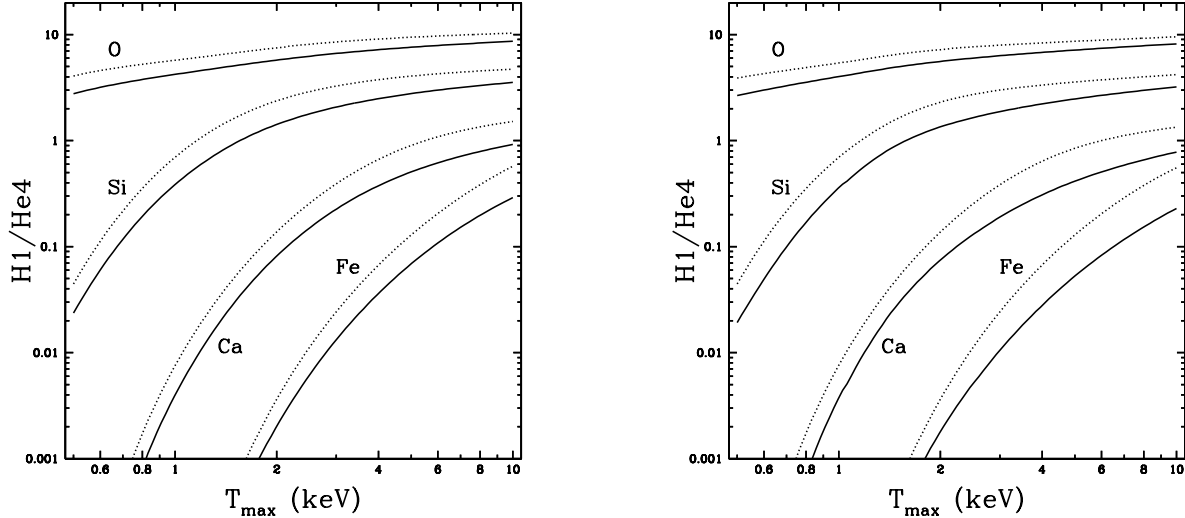


Figure 9. H1/He4 ratios for selected elements in models with a constant pressure cooling flow (left) and isothermal sphere cooling flow with $\dot{M} \propto r$ (right). In each case the line ratios for the cooling flows are given by solid lines while composite models consisting of a cooling flow and a single temperature component (each with equal total emission measure) are given by the dotted lines. All models have $Z = 0.5Z_{\odot}$ and relative abundances are fixed at the (photospheric) solar values.

The H1/He4 line ratios for both the isothermal sphere cooling flow component and a composite model of an isothermal sphere cooling flow component with a single temperature component (all with $Z = 0.5Z_{\odot}$) are plotted along side the corresponding constant pressure models in Figure 9. For the case of only a cooling flow the line ratios are very similar, especially for $T_{\max} \lesssim 2$ keV. The greatest discrepancies between the isothermal and constant-pressure cases are seen at the largest temperatures for the lines with the highest energies; e.g. the Fe H1/He4 ratios differ by ~ 40 per cent for $T_{\max} = 10$ keV. Adding the single temperature to the isothermal cooling flow has a slightly larger effect than found for the constant pressure cooling flow. However, the composite models of the isothermal and constant pressure cases actually differ from each other by $\lesssim 10$ per cent over the entire temperature range shown. (Note that the line ratios for models with $Z = 2Z_{\odot}$ differ by essentially the same small amounts described above for the constant pressure models.)

2.3 Distinguishing a two-temperature plasma from a cooling flow

We have seen in the previous section that for a particular value of a line ratio (e.g. Si H1/He4) the two-temperature models appear to have a larger variety of possible σ_{ξ} which can produce a line ratio in comparison to the simple continuous emission measure models examined. As a result, for moderate resolution spectra like ASCA (Tanaka et al. 1994) where at most only a limited number of line blends are resolved, it should be expected that a two-temperature model can provide an acceptable fit even if the true spectrum is that of a cooling flow. In fact, analyses of ASCA spectra of the brightest ellipticals (Buote & Fabian 1998; Buote 1999a), poor groups (Buote 1999b), and clusters of galaxies (e.g. Fabian et al. 1994a) have found that two-temperature models and models composed of a cooling flow with an ambient

temperature component essentially describe the data equally well.

To examine how to distinguish between the two-temperature and cooling flow models we first examine the case of the bright elliptical galaxy NGC 4472. In Table 4 we list the results of the best-fitting two-temperature and cooling flow models to the ASCA spectra accumulated within a radius of ~ 30 kpc from the center of NGC 4472 by Buote (1999a). The “2T+Bremsstrahlung” model consists of two MEKAL plasma components and one component of thermal bremsstrahlung to account for possible emission from discrete sources; T_c and T_h represent the temperatures of the “cooler” and “hotter” MEKAL components respectively. The “CF+1T+Bremsstrahlung” model replaces the cooler MEKAL component with a constant pressure cooling flow component (equation 8). Each model component is modified by photoelectric absorption (Balucińska-Church & McCammon 1992) although the absorption on the bremsstrahlung components is fixed to the Galactic value. We refer the reader to Buote (1999a) for full details of these models.

In Figure 10 we plot a selection of line ratios computed from the models in Table 4. (We show a related plot of the ratios of the spectra of two temperature and cooling flow models in Figure 18 in Section 4.2.) Overall, it is remarkable how similar the line ratios are for the two models. The O H1/He4 and Fe L ratios show the most differences between the two-temperature and cooling flow models; i.e. the O H1/He4 ratios differ by a factor of ~ 4 and the 2:1 Fe L ratios differ by a factor of ~ 2 . The ratios shown involving other elements differ by $\lesssim 10$ per cent. Note that we expect the H1/He4 ratio of Si to be similar for the models since the blends involving the He4 and H1 transitions are reasonably resolved by ASCA (see next section) and thus the best-fitting models in Table 4 attempt to match the observed Si ratio as accurately as possible.

For comparison to NGC 4472 where the cooling flow component dominates the emission measure and $T_{\max} < 2$

Table 4. Spectral Models for NGC 4472 and the Centaurus Cluster

Model	N_{H}^{c} (10^{21} cm^{-2})	N_{H}^{h} (10^{21} cm^{-2})	T_{c} (keV)	T_{h} (keV)	Z (Z_{\odot})	EM_{c} (10^{65} cm^{-3})	EM_{h} (10^{65} cm^{-3})	\dot{M} ($M_{\odot} \text{ yr}^{-1}$)	T_{B} (keV)	EM_{B} (10^{65} cm^{-3})	σ_{ξ}
NGC 4472:											
2T+BREM	2.9	0.04	0.72	1.39	2.00	0.065	0.050	...	3.23	0.0069	0.44
CF+1T+BREM	2.9	0.00	1.30	1.30	1.41	0.185	0.032	2.54	3.71	0.0045	0.03
Centaurus:											
2T	2.3	1.4	1.04	3.07	1.10	1.41	17.0	0.02
CF+1T	3.0	1.3	3.30	3.30	1.19	2.45	11.8	45.4	0.11

Best-fitting spectral models to *ASCA* data for the elliptical galaxy NGC 4472 and for the Centaurus cluster. The CF components are constant pressure cooling flow models, the 1T components are single-temperature MEKAL models, and B stands for a bremsstrahlung component. See text for further explanation of these models. The emission measures are computed using the distances described in the notes to Table 6. (Note that σ_{ξ} for the 2T and 2T+BREM models is actually σ_{ξ}^N evaluated for $N_c = 20$.)

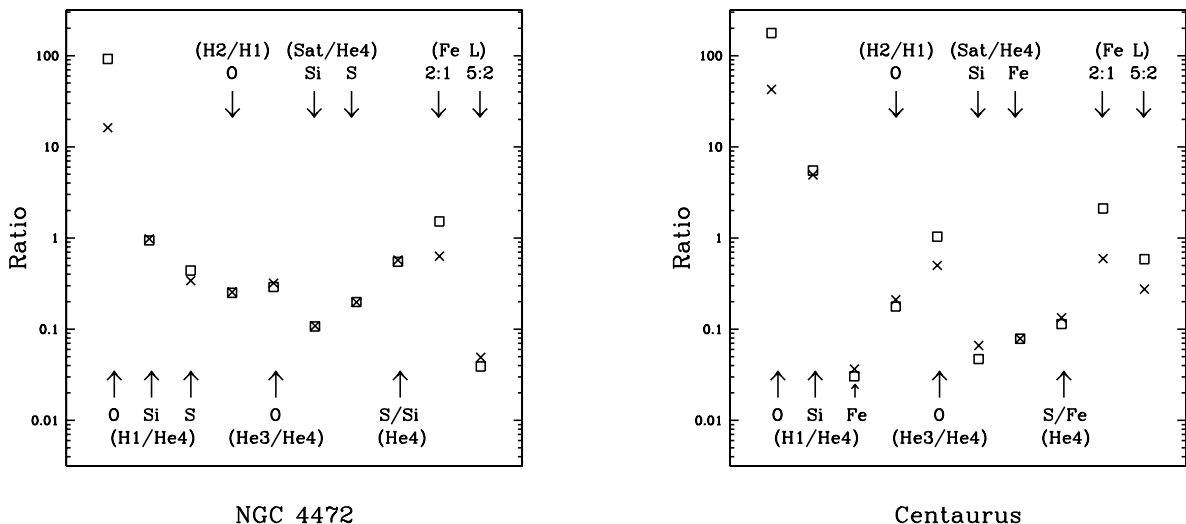


Figure 10. Selected line ratios of two-temperature models (boxes) and models consisting of a cooling flow and a single temperature (crosses) for NGC 4472 and Centaurus (see Table 4). (Note that the line ratios are computed as described in Section 2 except that the absorption is included.)

keV we consider the Centaurus cluster of galaxies. In Table 4 we list the best-fitting 2T and CF+1T models to the *ASCA* data accumulated within a radius of ~ 100 kpc. The details of the data reduction and spectral fitting follow those in section 3 with the following important exceptions. Firstly, we fitted the *ASCA* SIS spectra over the energy range 0.5–9. keV. Secondly, we used the photospheric solar abundances according to Anders & Grevesse (1989) because of our current implementation of the cooling flow model for use in XSPEC (Arnaud 1996) is defined for those solar abundances. Although this restriction limits the quality of the fits, the 2T and CF+1T models give very similar quality fits which is all that we require for this discussion. We refer the reader to section 3 for a thorough discussion of successful spectral models of Centaurus.

In contrast to NGC 4472 the isothermal component dominates the emission measure of the cooling flow model for Centaurus, $EM_{\text{h}}/EM_{\text{c}} \approx 5$. Nevertheless, the CF+1T model has $\sigma_{\xi} = 0.11$ indicating that it is significantly multi-phase (see previous section). We plot selected line ratios of the 2T and CF+1T models in Figure 10. Since Centaurus has a higher temperature than NGC 4472, in the figure we

replace the S H1/He4 and Sat/He4 ratios with the corresponding Fe ratios; S/Si (He4) is replaced with S/Fe (He4). (Again, we show a related plot in Figure 18 in Section 4.2.) Similar to NGC 4472 the O H1/He4 and Fe L ratios show the most substantial differences (factors of ~ 5). However, unlike NGC 4472 the O He3/He4 and Si Sat/He4 show noticeable differences. (The Sat/He4 ratios of S, Ar, and Ca have quite similar differences as well.) Again the Si H1/He4 ratios are very similar for the three models because the Si H1/He4 ratio is a key constraint of the *ASCA* spectral fits.

Hence, the most substantial differences between two-temperature and cooling flow models occur for O and Fe L line ratios. Analyses that exclude energies below 1.4 keV (e.g. to avoid small inaccuracies in the plasma codes) will have a very difficult time differentiating two-temperature and cooling flow models, particularly for moderate spectral resolution data provided by *ASCA*, *Chandra*, and *XMM*. Moreover, because of their overall flexibility, an observed consistency of a two-temperature model with data of low-moderate spectral resolution of ellipticals, groups, and clusters should not be regarded as decisive evidence that the system has only two phases.

Table 5. Energy Ranges of ASCA Line Blends

Dominant Ion	Energy Range (keV)
Si XIII	1.80 - 1.90
Si XIV	1.95 - 2.05
S XV	2.35 - 2.53
S XVI	2.55 - 2.70
Ar XVII	3.00 - 3.25
Ar XVIII	3.25 - 3.40
Fe XXV	6.40 - 6.80
Fe XXVI	6.86 - 7.14
7.8 keV Blend	7.60 - 8.10

Energy ranges used to define the lines in Figure 11 appropriate for the energy resolution of the ASCA SIS during approximately 1994.

3 APPLICATION TO ASCA DATA

Recently the ASCA satellite is able to resolve emission line blends of K shell transitions of Mg, Si, S, Ar, Ca, and Fe, and also has the effective area and imaging capabilities lacking in previous X-ray satellites having similar or better spectral resolution. The energy resolution of ASCA (e.g. $\Delta E \sim 100$ eV FWHM at 2 keV) allows only blends of lines to be measured, and we show in Figure 11 the temperature profiles of ratios of the most important line blends relevant to ASCA observations of ellipticals, groups, and clusters; the definitions of the blends are given in Table 5. These profiles should be compared to Figure 3.

Even though they are the most powerful diagnostics of multiphase cooling flows (see Section 2.3), we do not show oxygen or Fe L blends in Figure 11 for the following reasons. The strongest transitions of the He-like O VII ion appear at energies ~ 0.57 keV which lie in a region where the ASCA SIS have small effective area and problems with the calibration. The energy resolution of ASCA does not allow useful separation of blends of Fe L lines between ~ 0.7 - 1.4 keV for individual analysis. This is not crucial to our present analysis since it is our intention to investigate the K shell emission lines which do not suffer from the possible inaccuracies in the plasma codes associated with the Fe L shell transitions.

As indicated by the discussion in Section 2.3 line ratios other than those of oxygen or Fe L in rival multiphase models generally differ by only ~ 10 - 20 per cent. Only a handful of ASCA observations of the brightest ellipticals, groups, and clusters have sufficient S/N to even approach this level of precision. The $K\alpha$ line blends of both H-like and He-like Si and S have been analyzed with ASCA by Buote (1999a) for three of the brightest elliptical galaxies (NGC 1399, 4472, and 4636) and one of the brightest galaxy groups (NGC 5044). Although the properties of these line blends favor multitemperature models obtained from broad-band (0.5-9 keV) fits to the ASCA spectra, the line blends are not measured precisely enough to place interesting constraints on $\xi(T)$ by themselves.

Clusters of galaxies are hotter and more luminous than ellipticals and groups, and thus the K shell emission lines above ~ 2 keV in principle can be measured more precisely for the brightest clusters. Let us consider the bright nearby clusters M87 (Virgo), Centaurus (A3526), and Perseus (A426) which have among the highest S/N data available for clusters observed with ASCA. Broad-band

spectral fitting of the ASCA data (which includes the Fe L lines) has shown that at least two temperature components are required in the cores of each of these clusters (Fabian et al. 1994a; Fukazawa et al. 1994; Matsumoto et al. 1996). It is our intention to examine what can be learned from analysis of only the K shell emission line blends and, in particular, to examine whether they too require multiple temperature components in M87, Centaurus, and Perseus.

3.1 ASCA observations and data reduction

The ASCA satellite consists of two X-ray CCD cameras (Solid State Imaging Spectrometers – SIS0 and SIS1) and two proportional counters (Gas Imaging Spectrometers – GIS2 and GIS3) each of which is illuminated by its own X-ray telescope (XRT). The SIS has superior energy resolution and effective area below ~ 7 keV while the GIS has a larger field of view. Although the point spread function (PSF) of each XRT has a relatively sharp core, the wings of the PSF are quite broad (half power diameter $\sim 3'$) and increase markedly for energies above a few keV (e.g. Kunieda et al. 1995). As in our previous studies we do not attempt to analyze the spatial distribution of the ASCA data of these sources because of the large, asymmetric, energy-dependent PSF. Rather, we analyze the ASCA X-ray emission within a single large aperture for each cluster which encloses the region of the brightest emission (see below). For clusters of galaxies the spectrum within this central region is not very much affected by scattered emission from large radii (e.g. Boehringer et al. 1998).

We obtained ASCA data for the clusters from the public data archive maintained by the High Energy Astrophysics Science Archive Research Center (HEASARC). The properties of the observations are listed in Tables 6 and 7. We reduced these data with the standard FTOOLS (v4.1) software according to the procedures described in The ASCA Data Reduction Guide and the WWW pages of the ASCA Guest Observer Facility (GOF)**.

For the observations of M87 and Perseus (taken during the Performance-Verification phase) we used the events files generated by the default screening criteria processed under the Revision 2 Data Processing (REV2). As is standard procedure for analysis of SIS data, only data in BRIGHT mode taken in medium or high bit rate were used. Since the Centaurus observation was performed in 1995 its SIS data are degraded to some extent because of radiation damage to the CCDs (see Dotani et al. 1997). We corrected the Centaurus data for this “RDD effect” following the procedure outlined on the ASCA GOF WWW pages which produces corrected SIS event files in BRIGHT2 mode constructed using the default REV2 screening criteria. (Again, only data with medium or high bit rate were used.) Since we focus on energies above 1.6 keV this correction is actually not very important for our study.

Our final screening of the data involved visual examination of the light curves for each observation and removing intervals of anomalously high (or low) count rate. We note that only data with the standard events grades (0234) were

** See <http://heasarc.gsfc.nasa.gov/docs/asca/abc/abc.html> and <http://heasarc.gsfc.nasa.gov/docs/asca/>.

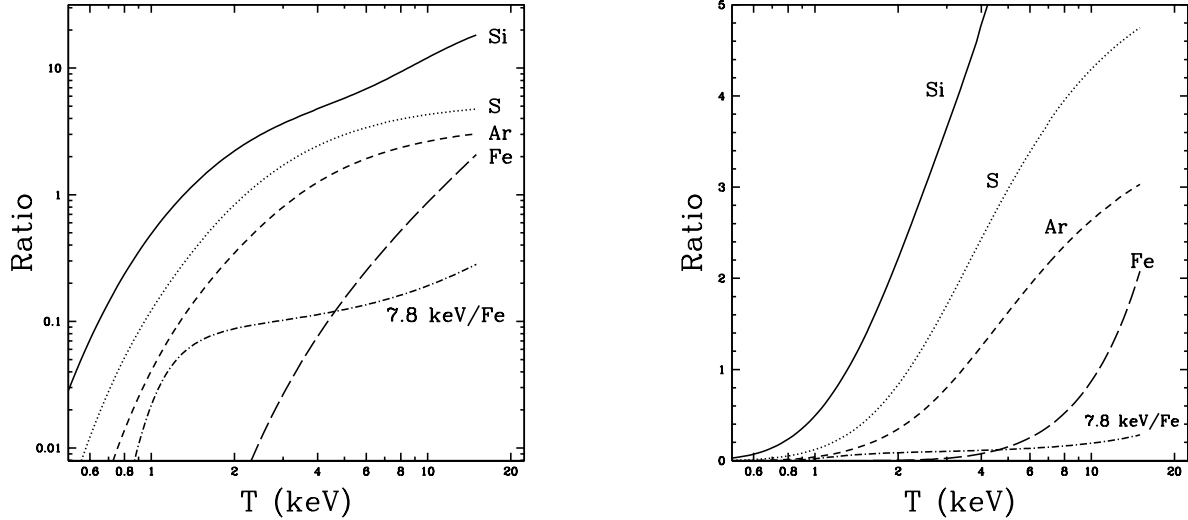


Figure 11. (Left) Line ratios as a function of temperature in isothermal MEKAL models (with $Z = 0.5Z_{\odot}$) where the emission lines have been computed over large energy ranges appropriate for the energy resolution of ASCA (see Table 5). The ratios for Si, S, Ar, and Fe refer to ratios of H-like to He-like K α transitions as in Figure 3 except that now additional transitions are included in the blends. The 7.8 keV blend consists mostly of K β Fe XXV (He3) although K α emission from Ni XXVII and Ni XXVIII contribute as well. (Right) The same thing but plotted on a linear scale.

Table 6. Cluster Properties and ASCA Observations

Cluster	z	N_{H} (10^{21} cm^{-2})	Sequence	Date Mo/yr	SIS Mode	SIS Mode	RDD Correction	Radius (arcmin)	Radius (kpc)		
					CCD	Data		SIS	GIS	SIS	GIS
M87	0.0043	0.25	60033000	6/93	4	BRIGHT	N	6.2	7.5	32.5	39.3
Centaurus	0.0110	0.81	83026000	7/95	1	BRIGHT2	Y	5.6	6.5	77.2	89.6
Perseus	0.0183	1.41	80007000	8/93	4	BRIGHT	N	5.6	6.3	128.7	144.8

Selected properties of the ASCA SIS and GIS observations. Galactic Hydrogen column densities (N_{H}) are from Dickey & Lockman (1990) using the HEASARC w3nh tool. Extraction radii in kpc are computed using luminosity distances of 18 Mpc for M87, 47 Mpc for Centaurus, and 79 Mpc for Perseus assuming $H_0 = 70 \text{ km s}^{-1} \text{ Mpc}^{-1}$ and $\Omega_0 = 0.3$.

used, and we made the required dead time corrections for the GIS data.

The final processed events were then extracted from a region centered on the emission peak for each detector of each sequence. We selected a particular extraction region using the following general guidelines. Our primary concern is to select a region that encloses most of the X-ray emission yet is symmetrically distributed about the origin of the region. We limited the size of the aperture to ensure that the entire aperture fit on the detector, an issue more important for the SIS because of its smaller field-of-view. Moreover, for the SIS0 and SIS1 we tried to limit the apertures to as small a number of chips as possible to reduce the effects of residual errors in chip-to-chip calibration. The GIS regions were chosen to be of similar size to the corresponding SIS regions of a given sequence for consistency. Since, however, the GIS+XRT PSF is somewhat larger than that of the SIS+XRT the extraction regions for the GIS are usually $\sim 20\%$ larger.

Since the SIS was operated in 1-ccd mode for the Centaurus observation we extracted all of the emission from that ccd which amounts to a square region with sides of $\sim 11'$ width. The observation of Perseus was positioned very near the center of the default chips of the SIS and so we also extracted its SIS data from the whole chip. The observa-

tion of M87 was centered between two chips, and thus we used a circular region. In Table 6 we list the region sizes for the SIS and GIS data of each cluster. For the SIS data of Centaurus and Perseus the radii actually are half-widths of the default ccds. (Note that the data between the ccds are excluded.) All of the GIS radii refer to circles. We extracted the events using regions defined in detector coordinates as is recommended in the *ASCA ABC GUIDE* because the spectral response depends on the location on the detector not the position on the sky.

We computed a background spectrum for each detector using the standard deep observations of blank fields. It is necessary to use these background templates because the cluster emission fills the entire field of view in each case. The background templates for the SIS are most appropriate for SIS data taken in 4-ccd mode early in the mission which applies to the M87 and Perseus observations. For more recent data taken in 1-ccd or 2-ccd mode, using these background templates can lead to spurious effects particularly for energies above ~ 7 keV where instrumental background dominates the cosmic X-ray background. The Centaurus observation was performed in 1995 and thus these effects are not expected to be as serious as for more recent data. At any rate, the Centaurus data are not dominated by background so small systematic effects in the background should not be

Table 7. ASCA Exposures and Count Rates

Cluster	Exposure		Count Rate		Exposure		Count Rate	
	(10 ³ s)	(10 ³ s)	(ct s ⁻¹)	(ct s ⁻¹)	(10 ³ s)	(10 ³ s)	(ct s ⁻¹)	(ct s ⁻¹)
M87	12.8	9.79	2.59	1.87	16.7	16.7	2.33	2.39
Centaurus	64.6	64.4	1.22	0.94	70.8	70.8	0.86	1.06
Perseus	16.1	16.1	7.15	6.16	15.0	14.9	5.53	6.62

Exposures include any time filtering. The 1.6-9 keV count rates are background-subtracted within the particular aperture (see Table 6).

apparent in our analysis. The final screened background-subtracted exposures and count rates are listed in Table 7.

The instrument response matrix required for spectral analysis of ASCA data is the product of a spectral Redistribution Matrix File (RMF) and an Auxiliary Response File (ARF). The RMF specifies the channel probability distribution for a photon (i.e. energy resolution information) while the ARF contains the information on the effective area. An RMF needs to be generated specifically for each SIS of each observation because, among other reasons, each chip of each SIS requires its own RMF and the spectral resolution of the SIS is degrading with time. We generated the responses for each SIS using the FTOOL SISRMG selecting for the standard event grades (0234). Using the response matrix and spectral PI (Pulse Invariant) file we constructed an ARF file with the FTOOL ASCAARF.

The source aperture used for the SIS overlapped more than one chip for M87. In order to analyze the spectra of such regions we followed the standard procedure of creating a new response matrix that is the average of the individual response matrices of each chip weighted by the number of source counts of each chip (i.e. within the source aperture). (Actually, the current software only allows the RMFs to be averaged and then an ARF is generated using the averaged RMF. This is considered to be a good approximation for most sources.) Unfortunately, some energy resolution is lost as a result of this averaging.

Since the K shell emission lines for energies above ~ 2 keV are relatively faint in these clusters we maximize the S/N of the data by combining the spectra from each SIS and similarly for each GIS; i.e. SIS=SIS0+SIS1 and GIS=GIS2+GIS3. For the GIS data this does not result in significant loss of information because the RMFs of the GIS2 and GIS3 are the same and time-independent; only the ARFs need to be averaged for the GIS2 and GIS3. However, the responses of the SIS0 and SIS1 detectors are different and thus the required averaging of the RMFs and ARFs leads again to loss of information. Because the gain in S/N is important for our study, we examine the combined SIS and combined GIS data of each cluster where the source spectra, RMF, ARF, and background for each detector are summed and scaled appropriately using the FTOOL ADDASCASPEC (v1.27).

Overall we found that the results obtained from analysis of these summed SIS spectra agreed very well with results obtained without summing the data. Henceforth we shall focus on results obtained from the summed SIS data though we will (for completeness) mention some of the results obtained from separate analysis of the SIS0 and SIS1 data.

3.2 Analysis of individual emission line blends

We focus our analysis of individual line blends on the SIS data because, unlike the GIS, the SIS is able to resolve both the He-like and H-like blends of the K shell lines of the abundant elements (e.g. see Figure 1 of Buote 1999a). The GIS data can provide useful supplementary constraints on the continuum for energies above ~ 5 keV which we mention below.

Our procedure for obtaining the properties of the line blends commences by fitting a thermal bremsstrahlung model to represent the continuum emission. We desire a measurement of the local continuum near the line blends of interest so that the assumption of a single temperature is reasonable even if the spectrum actually consists of multiple temperature components. However, because of S/N considerations and the finite energy resolution of the SIS we allowed the continuum component to extend over multiple line blends that are nearby in energy. The line blends of interest were then modeled as Gaussians of zero intrinsic width on top of the continuum component.

We fitted only line blends that are either obvious from visual inspection of a spectrum or significantly improved the fit as judged in terms of χ^2 . All spectral fitting was performed with the software package XSPEC (Arnaud 1996). In order for the weights to be valid for the χ^2 method we followed the standard procedure and regrouped the PI bins for each source spectrum so that each group had at least 20 counts. The background templates also generally have at least 20 counts when their energy bins are grouped similarly to the source spectra. The background-subtracted count rate in a particular group can be small, but the uncertainties in the source and background are correctly propagated by XSPEC to guarantee approximately gaussian statistics for the statistical weights (K. Arnaud 1998, private communication).

The energies of the lines were free parameters in the fits. When determining the error bars on the equivalent widths and fluxes for a particular line the energies of the other lines were fixed at their best-fitting values. This was done to insure that the other lines did not mix during the error search.

3.2.1 Properties of $K\alpha$ and $K\beta$ lines

In Table 8 we summarize the properties of the line blends measured from the summed SIS data. The spectral regions and best-fitting models used to measure the line properties are displayed for each cluster in Figures 12-14.

We detect most of the strong $K\alpha$ lines of the abundant elements lying between the energies 1.6 and 9 keV in each cluster. In Centaurus both the H- and He-like $K\alpha$ line

Table 8. Emission Lines Measured from ASCA Data

Ion	<i>E</i> (keV)	<i>T</i> (keV)	EW (eV)	Flux (10^{-5} ph cm $^{-2}$ s $^{-1}$)	Flux (10^{-13} erg cm $^{-2}$ s $^{-1}$)
M87:					
Mg XII (H)	$1.48^{+0.01}_{-0.01}$	$1.06^{+0.18}_{-0.14}$	28^{+6}_{-5}	$62.86^{+11.07}_{-10.99}$	$14.86^{+2.62}_{-2.60}$
1.7 keV Feature	$1.74^{+0.02}_{-0.02}$	$1.23^{+0.29}_{-0.21}$	13^{+6}_{-6}	$19.91^{+9.16}_{-9.17}$	$5.54^{+2.55}_{-2.55}$
Si XIII (He)	$1.84^{+0.01}_{-0.01}$	$1.23^{+0.29}_{-0.21}$	54^{+9}_{-8}	$68.68^{+9.49}_{-9.34}$	$20.29^{+2.80}_{-2.76}$
Si XIV (H)	$1.99^{+0.00}_{-0.00}$	$1.23^{+0.29}_{-0.21}$	110^{+17}_{-16}	$110.40^{+11.22}_{-11.00}$	$35.26^{+3.58}_{-3.51}$
2.2 keV Feature	$2.18^{+0.02}_{-0.01}$	$1.23^{+0.29}_{-0.21}$	28^{+16}_{-14}	$21.94^{+10.07}_{-9.97}$	$7.66^{+3.52}_{-3.48}$
S XV (He)	$2.44^{+0.01}_{-0.01}$	$2.19^{+0.89}_{-0.50}$	68^{+14}_{-13}	$47.25^{+7.84}_{-7.94}$	$18.49^{+3.07}_{-3.11}$
S XVI (H)	$2.60^{+0.01}_{-0.01}$	$2.19^{+0.89}_{-0.50}$	68^{+12}_{-11}	$40.52^{+6.17}_{-6.17}$	$16.90^{+2.57}_{-2.57}$
Ar XVII (He)	$3.09^{+0.02}_{-0.02}$	$2.43^{+0.22}_{-0.19}$	44^{+12}_{-12}	$16.86^{+4.41}_{-4.38}$	$8.35^{+2.18}_{-2.18}$
*Ar XVIII (H)	$3.28^{+0.05}_{-0.05}$	$2.43^{+0.22}_{-0.19}$	11^{+7}_{-7}	$3.54^{+2.18}_{-2.27}$	$1.86^{+1.15}_{-1.19}$
Ca XIX (He)	$3.89^{+0.03}_{-0.03}$	$2.43^{+0.22}_{-0.19}$	43^{+15}_{-15}	$8.70^{+2.98}_{-3.04}$	$5.42^{+1.86}_{-1.90}$
Fe XXV (He)	$6.63^{+0.01}_{-0.02}$	$2.61^{+0.62}_{-0.45}$	1010^{+160}_{-147}	$32.57^{+4.09}_{-4.11}$	$34.61^{+4.35}_{-4.37}$
7.8 keV Feature	$7.82^{+0.15}_{-0.23}$	$2.61^{+0.62}_{-0.45}$	308^{+228}_{-204}	$5.02^{+3.19}_{-3.22}$	$6.29^{+4.03}_{-4.03}$
Centaurus:					
Mg XII (H)	$1.47^{+0.01}_{-0.01}$	$3.06^{+1.06}_{-0.64}$	27^{+4}_{-4}	$26.22^{+3.35}_{-3.34}$	$6.18^{+0.79}_{-0.79}$
Si XIII (He)	$1.81^{+0.01}_{-0.01}$	$1.61^{+0.24}_{-0.19}$	25^{+4}_{-4}	$16.52^{+2.30}_{-2.29}$	$4.78^{+0.66}_{-0.66}$
Si XIV (H)	$1.98^{+0.00}_{-0.00}$	$1.61^{+0.24}_{-0.19}$	83^{+8}_{-8}	$42.43^{+3.22}_{-3.22}$	$13.47^{+1.02}_{-1.02}$
2.2 keV Feature	$2.22^{+0.02}_{-0.02}$	$1.61^{+0.24}_{-0.19}$	34^{+13}_{-12}	$13.17^{+4.26}_{-4.36}$	$4.68^{+1.51}_{-1.55}$
S XV (He)	$2.44^{+0.01}_{-0.01}$	$2.97^{+1.08}_{-0.61}$	44^{+10}_{-9}	$16.52^{+3.01}_{-3.00}$	$6.45^{+1.18}_{-1.17}$
S XVI (H)	$2.60^{+0.01}_{-0.01}$	$2.97^{+1.08}_{-0.61}$	50^{+8}_{-7}	$16.09^{+2.14}_{-2.15}$	$6.71^{+0.89}_{-0.90}$
Ar XVII (He)	$3.09^{+0.02}_{-0.02}$	$4.12^{+0.41}_{-0.35}$	40^{+9}_{-9}	$8.58^{+1.78}_{-1.80}$	$4.25^{+0.88}_{-0.89}$
Ar XVIII (H)	$3.31^{+0.58}_{-0.52}$	$4.12^{+0.41}_{-0.35}$	22^{+8}_{-8}	$4.15^{+0.53}_{-1.78}$	$2.20^{+0.79}_{-0.79}$
Ca XIX (He)	$3.86^{+0.51}_{-0.58}$	$4.12^{+0.41}_{-0.35}$	26^{+9}_{-9}	$3.54^{+2.10}_{-0.87}$	$2.19^{+0.71}_{-0.72}$
Ca XX (H)	$4.04^{+0.07}_{-0.07}$	$4.12^{+0.41}_{-0.35}$	12^{+9}_{-8}	$1.53^{+1.09}_{-1.08}$	$0.99^{+0.70}_{-0.70}$
Fe XXV (He)	$6.63^{+0.01}_{-0.01}$	$4.37^{+0.85}_{-0.64}$	972^{+68}_{-62}	$33.81^{+1.83}_{-1.81}$	$35.89^{+1.94}_{-1.92}$
Fe XXVI (H)	$6.97^{+0.07}_{-0.07}$	$4.37^{+0.85}_{-0.64}$	41^{+21}_{-21}	$2.40^{+1.22}_{-1.22}$	$2.68^{+1.36}_{-1.37}$
7.8 keV Feature	$7.81^{+0.07}_{-0.10}$	$4.37^{+0.85}_{-0.64}$	211^{+84}_{-84}	$4.21^{+1.47}_{-1.58}$	$5.26^{+1.83}_{-1.97}$
8.4 keV Feature	$8.35^{+0.06}_{-0.06}$	$4.37^{+0.85}_{-0.64}$	241^{+126}_{-120}	$3.86^{+1.78}_{-1.83}$	$5.17^{+2.38}_{-2.45}$
Perseus:					
Mg XII (H)	$1.48^{+0.01}_{-0.01}$	$10.96^{+15.60}_{-4.27}$	13^{+3}_{-3}	$74.19^{+16.28}_{-15.07}$	$17.62^{+3.87}_{-3.38}$
1.7 keV Feature	$1.72^{+0.03}_{-0.02}$	$5.01^{+2.16}_{-1.15}$	9^{+4}_{-4}	$42.13^{+18.22}_{-18.20}$	$11.60^{+5.02}_{-5.01}$
Si XIII (He)	$1.84^{+0.14}_{-0.13}$	$5.01^{+2.16}_{-1.15}$	13^{+3}_{-3}	$54.43^{+61.35}_{-33.32}$	$16.02^{+3.38}_{-3.38}$
Si XIV (H)	$1.97^{+0.13}_{-0.15}$	$5.01^{+2.16}_{-1.15}$	27^{+4}_{-4}	$101.73^{+35.82}_{-58.79}$	$32.18^{+4.44}_{-4.42}$
2.2 keV Feature	$2.23^{+0.02}_{-0.01}$	$5.01^{+2.16}_{-1.15}$	25^{+7}_{-7}	$75.19^{+18.67}_{-18.88}$	$26.82^{+6.66}_{-6.73}$
S XVI (H)	$2.60^{+0.02}_{-0.01}$	$2.92^{+0.96}_{-0.61}$	20^{+5}_{-5}	$47.15^{+12.08}_{-11.92}$	$19.68^{+5.04}_{-4.97}$
*2.8 keV Feature	$2.83^{+0.03}_{-0.03}$	$2.92^{+0.96}_{-0.61}$	7^{+5}_{-5}	$13.23^{+9.53}_{-9.30}$	$6.00^{+4.32}_{-4.21}$
Ar XVII (He)	$3.10^{+0.03}_{-0.03}$	$5.90^{+0.62}_{-0.51}$	12^{+6}_{-5}	$21.08^{+8.86}_{-8.92}$	$10.45^{+4.39}_{-4.42}$
Ar XVIII (H)	$3.26^{+0.03}_{-0.04}$	$5.90^{+0.62}_{-0.51}$	12^{+5}_{-5}	$18.61^{+7.91}_{-7.94}$	$9.72^{+4.13}_{-4.15}$
Ca XIX (He)	$3.82^{+0.06}_{-0.07}$	$5.90^{+0.62}_{-0.51}$	10^{+6}_{-5}	$11.40^{+6.05}_{-5.97}$	$6.97^{+3.70}_{-3.65}$
Ca XX (H)	$4.04^{+0.04}_{-0.04}$	$5.90^{+0.62}_{-0.51}$	10^{+6}_{-6}	$9.32^{+5.46}_{-5.88}$	$6.03^{+3.54}_{-3.80}$
Fe XXV (He)	$6.59^{+0.01}_{-0.01}$	$5.71^{+0.61}_{-0.53}$	402^{+27}_{-27}	$157.71^{+9.22}_{-9.22}$	$166.55^{+9.73}_{-9.73}$
Fe XXVI (H)	$6.81^{+0.03}_{-0.03}$	$5.71^{+0.61}_{-0.53}$	69^{+14}_{-14}	$37.14^{+7.49}_{-7.46}$	$40.54^{+8.17}_{-8.15}$
7.8 keV Feature	$7.74^{+0.07}_{-0.06}$	$5.71^{+0.61}_{-0.53}$	61^{+37}_{-35}	$13.55^{+8.01}_{-7.68}$	$16.80^{+9.93}_{-9.52}$

Results of fitting thermal bremsstrahlung and Gaussian models to ASCA SIS data of ellipticals and clusters having the largest available S/N. Except for Fe XXV (He) the intrinsic widths of the Gaussians are set to zero. Lines that have the same continuum temperature, *T*, are cases where multiple gaussians are joined by one bremsstrahlung model. See text for additional details regarding the model fitting. Quoted errors are 90 per cent confidence on one interesting parameter except for those lines with an asterisk for which 68 per cent limits are quoted.

blends of Si, S, Ar, Ca, and Fe are detected. These lines are also detected in the other clusters except for S XV (He) in Perseus and for Ca XX (H) and Fe XXVI (H) in M87. Mg XII (H) is also detected in each case but we advise caution in interpreting the derived EWs and fluxes of this line because the nearby unresolved Fe L lines undoubtedly affect

our estimates of the local continuum and the flux arising from only Mg.

In addition to the expected strong K α lines we detect other significant lines in each cluster. We label these as “Features” in Table 8 because they tend to be weaker than the K α lines and, more importantly, some of these line features

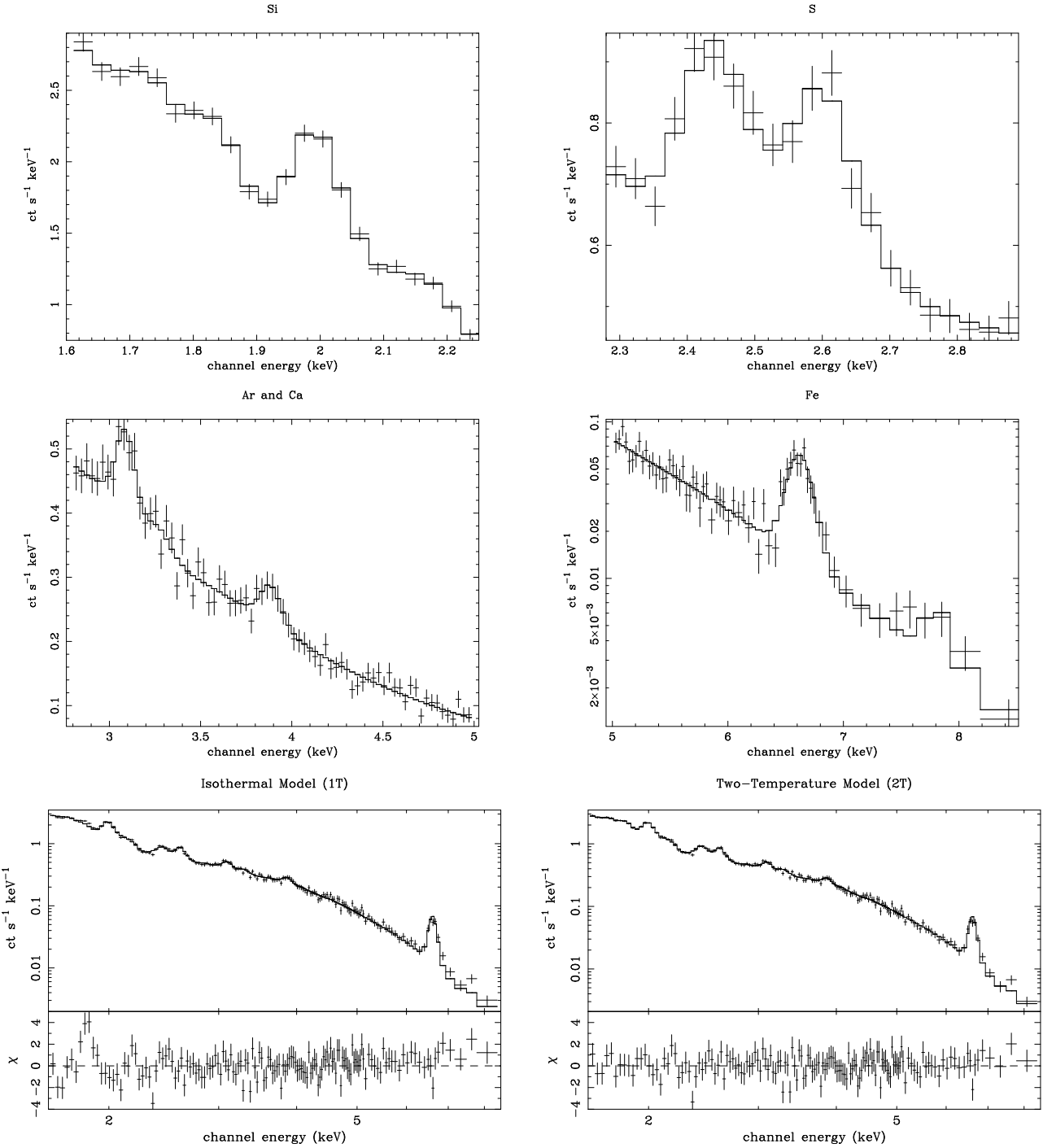


Figure 12. ASCA SIS spectral data for M87. The top four panels show the energy ranges and best-fitting Gaussian+continuum models used to obtain the line properties listed in Table 8. See text in section 3.2 for further explanation of these models. The bottom two panels show the best-fitting isothermal (left) and two-temperature (right) models fitted to the SIS data over 1.6–9 keV as listed in Table 10. These broad-band models are discussed in section 3.3.

may result in part or entirely from systematic errors in the SIS response. In particular, for each cluster we measure a significant line feature near 2.2 keV which in principle could be attributed to the 2.18 keV $K\beta$ line Si XIII (He3). However, this is precisely the location of a known calibration problem owing to the optical constants in the XRT (Gendreau & Yaqoob 1997) making it difficult to determine reliably the origin of the 2.2 keV features.

A significant line feature is also detected near 1.7 keV in M87 and Perseus. Assuming the feature is not instrumental then it is a blend of $K\beta$ Mg (H), $K\alpha$ Al (H), and some Fe L emission (see Figure 1). Although we are not aware of any problems currently in the SIS response near 1.7 keV, we stress that these features (and those at 2.2 keV) are not especially prominent (see Figures 12 and 14) and their existence is thus very dependent on the calibration.

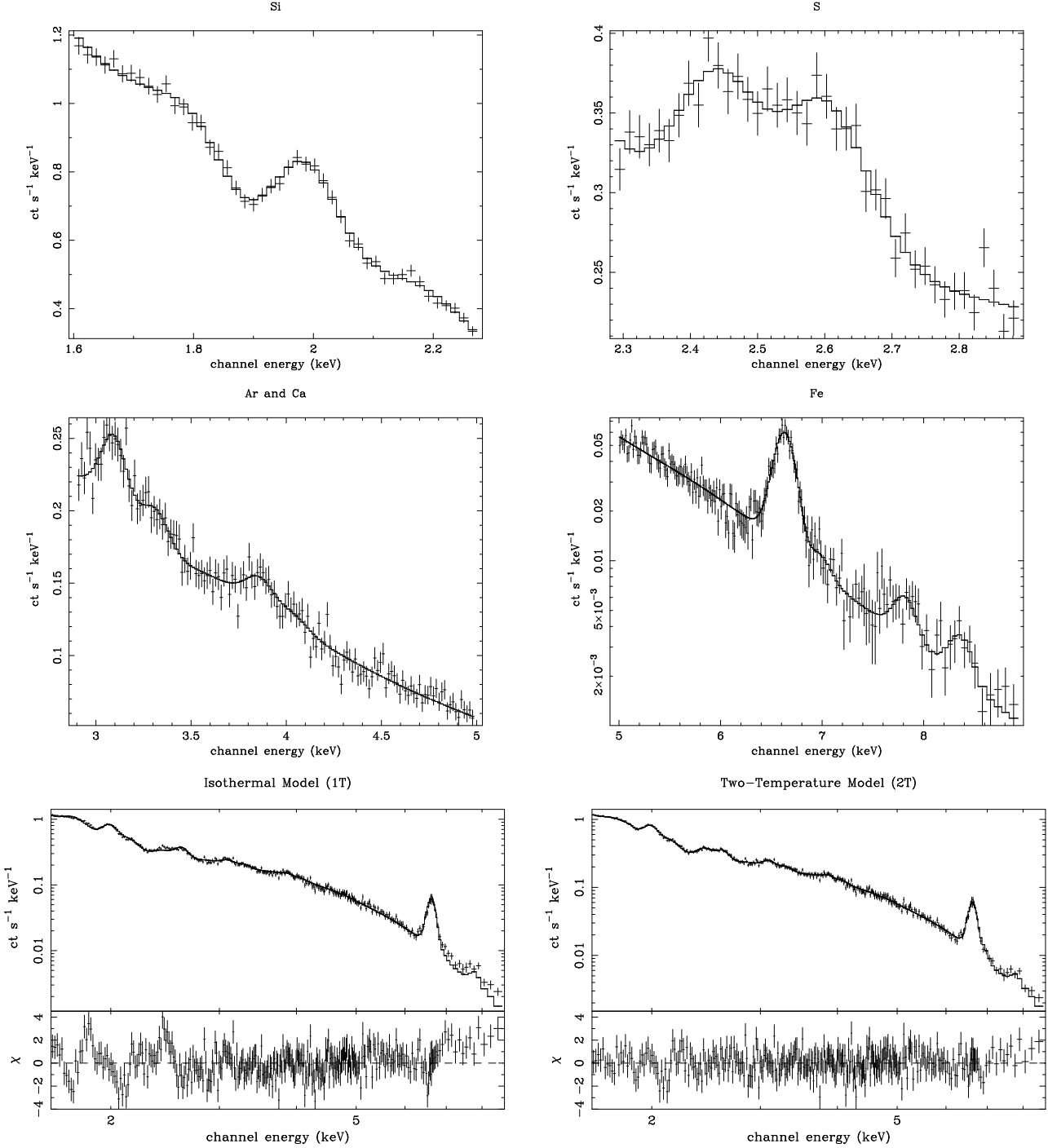


Figure 13. As Figure 12 but for Centaurus

In each cluster we also detect line features near 7.8 keV. If these features originate from hot plasma, they are primarily the result of K β emission from Fe XXV (He3) although some Ni K α should contribute as well. This feature is most prominent in Centaurus though it is clearly apparent to the eye in the SIS spectra of M87 (though it is noisy) and is least noticeable for Perseus (see below). Visual examination of the M87 spectrum (Figure 12) near 8 keV suggests that the line feature is broader than the instrumental resolution. A slightly better fit can be achieved either by adding another narrow Gaussian or by allowing the width of the sin-

gle Gaussian to take a non-zero value ($\sigma \sim 200$ eV). Since the parameters of these models are not well-constrained we prefer to present the results for the single Gaussian of zero width. (Also the other models imply continuum temperatures of ~ 2.2 keV which do not follow the trend of increasing continuum temperature with energy.)

Although no specific calibration features at 7.8 keV have been reported we do mention that there exist some calibration errors at high energies (i.e. above ~ 5 keV) due to the uncertainty in the optical axis, satellite wandering, and finite size of the Crab Nebula which is the key calibration source

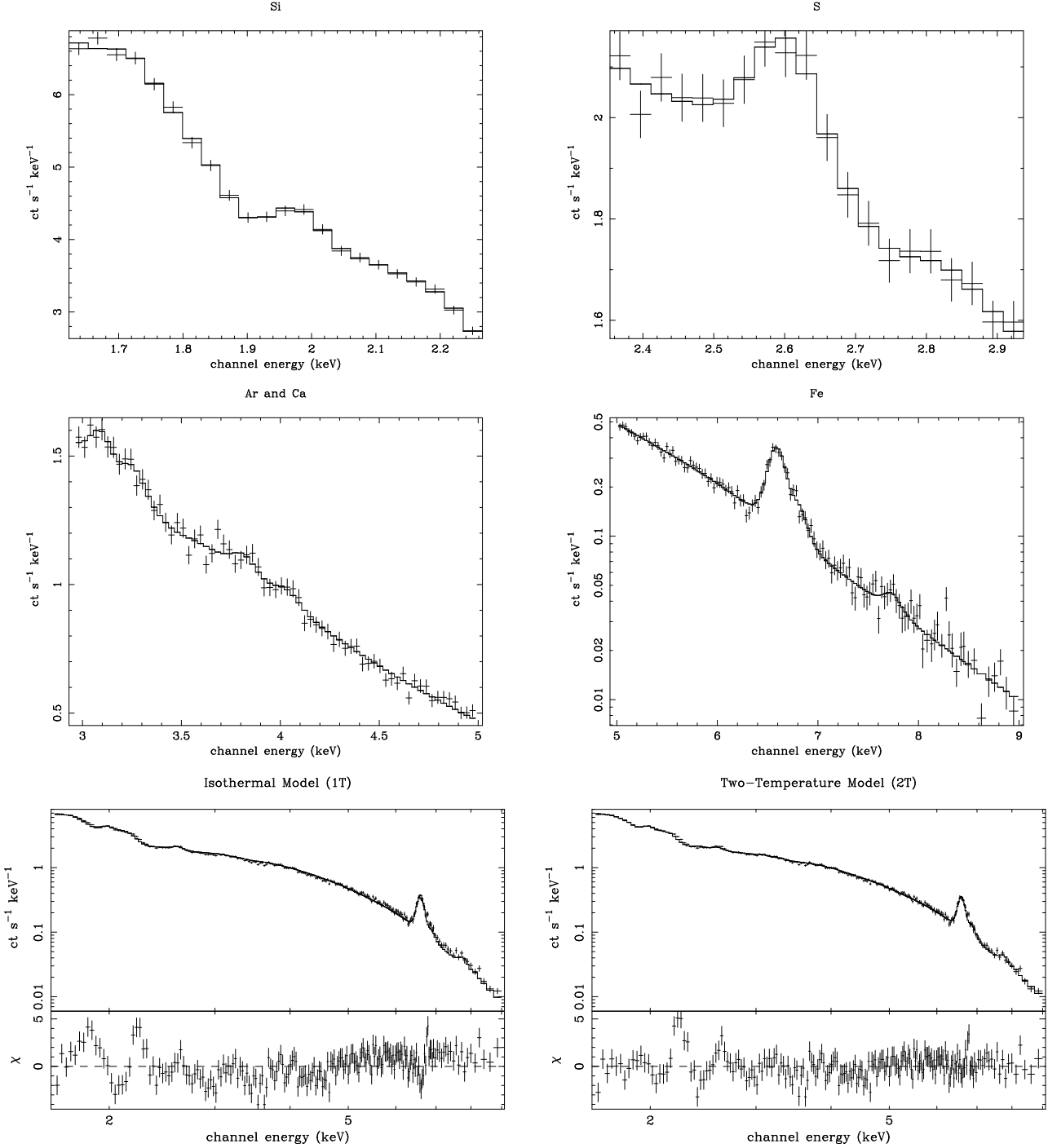


Figure 14. As Figure 12 but for Perseus.

(see Gendreau & Yaqoob 1997). These warnings also apply to the line feature detected at 8.4 keV for Centaurus which, if of plasma origin, implies higher order K shell transitions from Fe (see Figure 1).

Since the effects of calibration impact the various detectors differently, we have also measured the line properties for the SIS0 and SIS1 detectors separately. Generally we find excellent agreement for the line properties between the SIS0 and SIS1. The line fluxes are usually slightly larger for the SIS0, but the relative fluxes between the lines are generally consistent within the estimated 90 per cent errors for each

detector. Although the SIS0 and SIS1 results are generally consistent, some features are easier to see in the SIS0 data; e.g. 8.4 keV feature of Centaurus.

We have also verified the SIS results by simultaneously analyzing the SIS and GIS data. Only for the Fe K emission is some tangible improvement in the constraints offered by adding the GIS data. The key improvement is in the continuum temperature which is consistent with the values determined from the SIS data but typically has about half the statistical error. However, because the SIS and GIS responses differ we must let the line energies (as well as nor-

malizations) of both the SIS and GIS be free parameters in the fits (i.e. only the continuum temperature is tied between the detectors). The result is that adding the GIS does not appreciably improve the SIS constraints on the line fluxes.

Although the GIS also does not detect the Fe XXVI (H) line near 6.9 keV in Centaurus and Perseus because it is blended with the Fe XXV complex, we do confirm the features near 8 keV in M87 and Centaurus with the GIS. The GIS does not resolve the 7.8 and 8.4 keV features in Centaurus, but the parameters of two gaussian features obtained at those energies with the GIS agrees with the SIS results. Similar to the SIS the 7.8 keV “feature” in Perseus is not obvious from visual examination of the GIS spectrum, though similar constraints on the feature are achieved with the GIS. The principal reasons why we present results for a 7.8 keV line in Perseus are (1) because such a feature is required in M87 and Centaurus, and (2) for comparison to previous work (see below).

The results for the F XXV (He) line listed in Table 8 reflect a non-zero width on the Gaussian component. We obtained 90 per cent confidence σ values of $48.20^{+33.16}_{-19.86}$ eV for M87, $17.64^{+21.52}_{-17.64}$ eV for Centaurus, and $26.27^{+18.33}_{-26.27}$ eV for Perseus; i.e. σ is consistent with zero for Centaurus and Perseus. When analyzed separately we found that $\sigma \sim 60(30)$ eV for the SIS0 (SIS1) data for the Fe line of M87. Similarly, $\sigma \sim 24(7)$ eV for the SIS0 (SIS1) data of Perseus. For Centaurus the best-fitting $\sigma \sim 0$ eV for each SIS. The significant σ obtained for M87 may be due to finite intrinsic width of the Fe K complex, errors in the response matrix, or (most likely) a contribution to the emission from the (undetected) Fe XXVI (H) line.

Our results represent the first detections of many of the line blends in these clusters. The most complete catalogue of X-ray detections was previously reported by Matsumoto et al. (1996) who used *ASCA* SIS data to constrain the $K\alpha$ lines of H- and He-like Si and S as well as Fe XXV (He) for M87. Fukazawa et al. (1994) presented equivalent widths for the Si XIV (H), S XV (He), S XVI (H), and Fe XXV (He) lines which are consistent with our results (Table 8). Another notable paper is that of Molendi et al. (1998) who presented results for both the $K\alpha$ and $K\beta$ Fe XXV emission lines in the center of Perseus using data from the *SAX* satellite (Parmar et al. 1997). Therefore we have presented the first constraints on (1) individual Ar and Ca lines in each of these systems, (2) the H-like Fe XXVI lines in Centaurus and Perseus, and (3) Fe $K\beta$ emission in M87 and Centaurus. Our results for Mg XII (H) are also novel though our reported Mg flux is uncertain due to contamination from Fe L emission as noted above. However, it is reassuring that the energies of the fitted Mg lines lie exactly where Mg XII should be.

3.2.2 Temperatures from line ratios and local continuum

In Table 9 we list the temperatures implied by the H/He ratios of $K\alpha$ lines of the same element for each element where 90 per cent confidence limits on the fluxes are reported in Table 8. Recall that for isothermal gas these ratios are very temperature sensitive (Figure 3) and are independent of the elemental abundances. At the end of this section we shall also consider the temperatures suggested by the Fe $K\beta$ lines. Since the temperatures listed in Table 9 are not obtained by fitting plasma models directly to the data they should be

regarded as estimates which are sufficient for the qualitative discussion we present in this section. A quantitative assessment of the goodness-of-fit of different spectral models is given below in section 3.3.

For M87 the plasma temperature indicated by the Si ratio is ~ 1.7 keV while the S ratio gives $T \sim 2.1$ keV. If the gas is isothermal then the temperature should be the same for the Si and S ratios. Instead the increase in temperature from the Si lines near ~ 2.0 keV to the S lines near ~ 2.5 keV indicates that the emission measure consists of at least two components where the cooler component dominates the energy spectrum for $E \lesssim 2$ keV while the hotter component dominates for higher energies. These results are also consistent with emission from a continuous range of temperatures where again the cooler components contribute most significantly to the Si ratios and the hotter components dominate the S ratio; note that for the integrated *ASCA* spectrum within the circular aperture a continuous range of temperatures would be consistent with, e.g., the sum of different temperature components at different radii for a single-phase gas, or the sum of different phases in a multiphase cooling flow.

The variation in local continuum temperature as a function of energy (Table 8) gives further support for multiple temperature components in the *ASCA* spectrum of M87; i.e. the continuum temperature varies from ~ 1.2 keV near Si to ~ 2.6 keV near Fe XXV. This variation in continuum temperature does not arise from an increasing proportion of bound-free emission since free-free emission dominates except near the strong Fe L lines near 1 keV (and for lower energies). Although the local continuum temperature is consistent with the S ratio, it is somewhat lower than the Si ratio. This difference for Si could be due to an inaccurate continuum estimate arising from unresolved lines or from other systematics in the method we use to infer continuum temperature and line fluxes (section 3.2). However, for a multiphase plasma it is not necessary that the local continuum temperature agree with the temperature inferred from a line ratio assuming an isothermal gas. We also remark that the continuum temperature can be affected by non-thermal components whereas the line ratios are determined only by the hot plasma.

Our results are not inconsistent with those obtained by Matsumoto et al. (1996) but a direct comparison of our results is not possible because they did not use a local continuum when computing their line properties. These authors also examined the spectra within annuli of $2'$ width which may have been too small since the *ASCA* PSF is $3'$ in half-power diameter. Nevertheless, within our $\sim 6'$ aperture Matsumoto et al. also found evidence for non-isothermal gas. They estimated that the continuum temperature increased from 2.1 to 2.3 keV within $\sim 6'$ which is similar to the temperature difference we infer from the Si and S line ratios.

The evidence for multiple temperature components is even stronger for Centaurus. The $K\alpha$ line ratios imply temperatures of ~ 2.4 keV over energies ~ 2 -3 keV, $T \sim 3$ keV near 4 keV, and $T \sim 4$ keV near 7 keV. The continuum temperature increases from $T \sim 1.6$ keV near 2 keV to $T \sim 4$ keV near 7 keV. The good agreement between the temperatures implied by the Fe line ratio and the continuum near 7 keV indicates that a high-energy non-thermal component

Table 9. Temperatures Implied by ASCA Line Ratios

Cluster	Si	S	Ar	Ca	Fe	Fe K β /K α
M87	1.7 $^{+0.3}_{-0.3}$	2.1 $^{+0.2}_{-0.2}$	9.3 $^{+5.8}_{-7.9}$
Centaurus	2.4 $^{+0.3}_{-0.3}$	2.2 $^{+0.3}_{-0.2}$	2.4 $^{+0.6}_{-1.1}$	3.1 $^{+0.7}_{-1.1}$	4.0 $^{+0.4}_{-0.8}$	6.9 $^{+3.4}_{-4.7}$
Perseus	1.9 $^{+0.4}_{-0.2}$...	3.3 $^{+0.9}_{-0.9}$	4.2 $^{+1.2}_{-1.5}$	5.9 $^{+0.5}_{-0.4}$	2.8 $^{+5.2}_{-1.6}$

Isothermal temperatures in units of keV corresponding to H/He flux ratios of the K α lines listed in Table 8; also displayed are the Fe K β /K α ratios where Fe K β refers to the 7.8 keV feature and Fe K α refers to the strong Fe XXV (He) line. For each line ratio we computed the (MEKAL) temperature appropriate for the resolution of the ASCA SIS as described in Figure 11. The error bars reflect 90 per cent confidence limits.

(e.g. AGN, discrete sources) does not dominate the continuum of Centaurus for energies \sim 5-9 keV.

Hence, the variation of continuum temperature with energy should reflect a related variation in the plasma temperature, and when considering these temperatures and those inferred from the line ratios we conclude that the SIS spectrum of Centaurus clearly requires multiple temperature components for the hot gas within the ASCA aperture. (As with M87 the slight differences between continuum and line ratio temperatures are expected for a general spectrum with multiple temperature component.) A variation in temperature between $T \sim$ 2-4 keV is consistent with the two-temperature models fitted to the broad-band ASCA spectra by Fukazawa et al. (1994).

The K α line ratios for Perseus give perhaps the strongest evidence for multitemperature hot gas of the three clusters in our sample. The \sim 2 keV temperature inferred from the Si ratio is significantly less than $T \sim$ 6 keV implied by the Fe ratio. Similar to Centaurus the excellent agreement between the temperatures of the Fe ratio and the continuum near 7 keV argues against a strong contribution from a high-energy non-thermal component typical of, e.g. an AGN. In contrast to Centaurus the local continuum temperatures of Perseus are nearly constant with $T \sim$ 5-6 keV over approximately 2-8 keV; the small glitch near S likely reflects a miscalculation of the continuum due to our inability to compensate for the undetected He-like S XV line and the calibration error near 2.2 keV due to the optical constants in the XRT (Gendreau & Yaqoob 1997).

This near-isothermality of the continuum is not inconsistent with the temperature variations implied by the K α line ratios in Perseus. If the hottest temperature components near 6 keV dominate the continuum it is still possible for weaker cooler components to contribute to the line emission at lower energies. For example, in Figure 2 we show that the H1 Si XIV line is \sim 5 times stronger for $T =$ 2 keV than for $T =$ 6 keV for an isothermal gas; i.e. a cooler component can give a significant contribution to the line emission even if the continuum is dominated by hotter components. Moreover, the cooler component contributes negligibly to the Fe K α ratio since the H1 Fe XXVI line is over 100 times stronger for $T =$ 6 keV than for $T =$ 2 keV (Figure 2). Thus, the K α line ratios provide the key evidence for multitemperature gas in Perseus within the ASCA aperture.

Finally, the ratios of K β /K α lines also probe the temperature of the gas (Figure 3) but since our estimates of the fluxes of these lines may be dominated by systematic errors (see section 3.2.1) we advise extra caution when interpreting K β /K α ratios. In particular, since the 2.2 keV features are probably dominated by systematic errors (Gendreau & Yaqoob 1997), and the ratios of the fluxes of these features

to those of the Si XIII (He) lines generally imply much larger temperatures than the other lines, we do not discuss these lines further. We also do not discuss the 1.7 keV features since (if of plasma origin) they are blends of lines of three different elements.

The remaining candidate K β lines are the 7.8 keV features. As indicated in Table 9 the Fe K β /K α ratios are not very well constrained and in each case give temperatures consistent with the (H/He) Fe K α ratio and/or the continuum temperature near 7 keV; note that the ratio “Fe K β /K α ” means the ratio of the flux of the 7.8 keV feature to that of the He-like Fe XXV line. For Centaurus the ratio of the flux of the 8.4 keV feature to that of the He-like Fe XXV line implies $T \sim$ 9 keV for the best-fitting line ratio, but the 90 per cent confidence lower limit is $T \sim$ 1.3 keV.

Hence, these Fe K β /K α ratios do not require anomalously high temperatures at the 90 per cent confidence level and thus do not implicate resonance scattering as suggested by Molendi et al. (1998) for Perseus from analysis of SAX data. Molendi et al. obtained an Fe K β /K α ratio of \sim 0.20 within $r = 6.4'$ which is about twice our value of \sim 0.10 within $r = 5.6'$. However, the energy resolution of SAX is poorer than the ASCA SIS and thus to make a fair comparison we need to add the H-like Fe XXVI flux to the Fe K α emission; this reduces our Fe K β /K α ratio to \sim 0.08 corresponding to $T \sim$ 1.7 keV. Although there may be systematic errors in the ASCA data at these high energies as we discussed in section 3.2.1 (see Gendreau & Yaqoob 1997), the agreement we have obtained between the continuum temperatures and the Fe K α ratio for Perseus argues against a large systematic error. Therefore, we conclude that the Fe K β /K α ratio in Perseus deduced from ASCA is consistent with optically thin plasma and that the large ratio found by Molendi et al. (1998) with SAX must be due to an unrecognized systematic error.

We mention that the Fe K β /K α results we have quoted assume a photospheric solar Ni/Fe ratio. If instead we use the meteoritic solar ratios (see section 3.3) we find that the temperatures inferred for the Fe K β /K α ratios in Table 9 are reduced by a modest amount (\approx 25 per cent). To raise the inferred temperatures it is necessary to reduce the Ni/Fe ratio. Because the uncertainties are large we find that the temperatures implied by the 7.8 keV/Fe K α ratios are consistent with the local continuum temperatures even for $Z_{\text{Ni}}/Z_{\text{Fe}}$ ratios as small as \approx 1/5 (meteoritic solar).

3.3 Broad-band spectral fitting

The line ratios provide strong evidence for multiple temperature components within the ASCA apertures in each cluster.

Table 10. Broad-Band ASCA Spectral Fits

T_c (keV)	T_h (keV)	EM_c (see notes)	EM_h (see notes)	PL (see notes)	Fe	Mg	Si	S	Ar	Ca
M87:										
1T: (193.5/142/2.7e-3) $2.16^{+0.04}_{-0.04}$...	$1.56^{+0.07}_{-0.07}$	$0.85^{+0.14}_{-0.13}$...	$1.12^{+0.11}_{-0.10}$	$0.87^{+0.10}_{-0.10}$	$0.51^{+0.17}_{-0.17}$	$0.81^{+0.31}_{-0.30}$
1T+PL: (156.6/141/0.18) $1.92^{+0.07}_{-0.07}$...	$1.37^{+0.10}_{-0.10}$...	$0.39^{+0.11}_{-0.12}$	$1.01^{+0.21}_{-0.18}$...	$1.14^{+0.14}_{-0.13}$	$0.94^{+0.13}_{-0.11}$	$0.68^{+0.21}_{-0.19}$	$1.12^{+0.39}_{-0.37}$
2T: (130.3/140/0.71) $1.06^{+0.23}_{-0.42}$	$2.48^{+0.23}_{-0.14}$	$0.36^{+0.22}_{-0.12}$	$1.25^{+0.16}_{-0.21}$...	$0.78^{+0.13}_{-0.13}$...	$1.09^{+0.15}_{-0.12}$	$1.01^{+0.12}_{-0.11}$	$0.68^{+0.21}_{-0.20}$	$0.90^{+0.34}_{-0.33}$
2T+PL: (125.8/139/0.78) $0.85^{+0.31}_{-0.35}$	$2.21^{+0.28}_{-0.14}$	$0.22^{+0.20}_{-0.06}$	$1.29^{+0.11}_{-0.18}$	$0.20^{+0.15}_{-0.19}$	$0.87^{+0.18}_{-0.15}$...	$1.16^{+0.16}_{-0.14}$	$1.04^{+0.13}_{-0.12}$	$0.72^{+0.21}_{-0.20}$	$0.99^{+0.37}_{-0.35}$
Constant ξ : (131.9/141/0.70) $2.19^{+0.05}_{-0.05}$	$2.54^{+0.24}_{-0.26}$	$1.56^{+0.07}_{-0.07}$	$0.75^{+0.13}_{-0.12}$...	$1.04^{+0.11}_{-0.10}$	$0.96^{+0.11}_{-0.11}$	$0.72^{+0.21}_{-0.20}$	$0.97^{+0.36}_{-0.35}$
Centaurus:										
1T: (489.1/301/3.9e-11) $3.23^{+0.05}_{-0.05}$...	$0.60^{+0.02}_{-0.02}$	$1.28^{+0.09}_{-0.10}$	$6.25^{+1.71}_{-1.70}$	$1.76^{+0.13}_{-0.14}$	$1.28^{+0.13}_{-0.13}$	$0.68^{+0.21}_{-0.21}$	$0.74^{+0.30}_{-0.32}$
1T+PL: (373.2/300/2.6e-3) $2.49^{+0.10}_{-0.10}$...	$0.39^{+0.04}_{-0.04}$...	$0.49^{+0.06}_{-0.07}$	$2.56^{+0.44}_{-0.36}$	$1.75^{+2.09}_{-1.75}$	$2.16^{+0.27}_{-0.22}$	$1.73^{+0.24}_{-0.21}$	$1.36^{+0.33}_{-0.27}$	$1.50^{+0.48}_{-0.44}$
2T: (295.0/300/0.57) $1.59^{+0.12}_{-0.12}$	$4.80^{+0.39}_{-0.35}$	$0.26^{+0.04}_{-0.04}$	$0.39^{+0.04}_{-0.04}$...	$1.24^{+0.09}_{-0.08}$...	$1.31^{+0.09}_{-0.09}$	$1.23^{+0.11}_{-0.10}$	$1.24^{+0.24}_{-0.23}$	$1.47^{+0.39}_{-0.39}$
2T+PL: (286.8/299/0.68) $1.56^{+0.17}_{-0.17}$	$4.09^{+0.64}_{-0.56}$	$0.21^{+0.06}_{-0.07}$	$0.33^{+0.06}_{-0.06}$	$0.22^{+0.10}_{-0.12}$	$1.55^{+0.26}_{-0.21}$...	$1.54^{+0.20}_{-0.09}$	$1.46^{+0.22}_{-0.19}$	$1.45^{+0.30}_{-0.28}$	$1.62^{+0.45}_{-0.42}$
Constant ξ : (303.2/301/0.45) $3.46^{+0.06}_{-0.06}$	$5.02^{+0.24}_{-0.24}$	$0.62^{+0.01}_{-0.01}$	$1.26^{+0.08}_{-0.08}$...	$1.39^{+0.10}_{-0.09}$	$1.34^{+0.11}_{-0.11}$	$1.14^{+0.22}_{-0.22}$	$1.27^{+0.34}_{-0.34}$
Perseus:										
1T: (367.8/167/3.7e-17) $4.62^{+0.07}_{-0.06}$...	$4.77^{+0.05}_{-0.05}$	$0.62^{+0.03}_{-0.03}$...	$1.03^{+0.15}_{-0.15}$...	$0.00^{+0.07}_{-0.00}$	$0.00^{+0.21}_{-0.00}$
1T+PL: (244.2/166/7.5e-5) $3.21^{+0.18}_{-0.17}$...	$2.59^{+0.27}_{-0.27}$...	$5.38^{+0.51}_{-0.55}$	$1.36^{+0.25}_{-0.20}$...	$1.44^{+0.23}_{-0.21}$...	$0.35^{+0.28}_{-0.26}$	$0.59^{+0.39}_{-0.37}$
2T: (176.4/165/0.26) $1.27^{+0.13}_{-0.12}$	$6.12^{+0.29}_{-0.26}$	$1.32^{+0.15}_{-0.17}$	$3.74^{+0.15}_{-0.15}$...	$0.70^{+0.04}_{-0.04}$...	$0.64^{+0.11}_{-0.10}$...	$0.51^{+0.26}_{-0.25}$	$0.70^{+0.38}_{-0.37}$
2T+PL: (168.8/164/0.38) $1.30^{+0.15}_{-0.13}$	$5.59^{+0.43}_{-0.47}$	$1.13^{+0.19}_{-0.21}$	$3.05^{+0.42}_{-0.42}$	$2.00^{+1.09}_{-1.13}$	$0.83^{+0.12}_{-0.09}$...	$0.77^{+0.15}_{-0.14}$...	$0.68^{+0.31}_{-0.29}$	$0.89^{+0.46}_{-0.43}$
Constant ξ : (183.8/166/0.16) 4.94	$9.03^{+0.36}_{-0.40}$	$4.91^{+0.08}_{-0.08}$	$0.76^{+0.04}_{-0.04}$...	$0.79^{+0.10}_{-0.10}$...	$0.37^{+0.21}_{-0.21}$	$0.55^{+0.32}_{-0.32}$

Best-fitting and 90 per cent confidence limits on one interesting parameter ($\Delta\chi^2 = 2.71$) for models fitted to the summed SIS data between 1.6-9 keV. The models are defined similarly to those in Table 4 with the following exceptions: (1) the values of χ^2 , dof, and the null hypothesis probability are listed in parentheses next to the model, (2) the emission measures (EM) are quoted in units of $10^{-15} n_e n_p V / 4\pi D^2$ similar to what is done in XSPEC, (3) PL indicates the normalization of the power-law model (photon index 1.7) at 1 keV in units of 10^{-2} photons cm $^{-2}$ s $^{-1}$ keV $^{-1}$, and (4) the abundances are quoted in terms of the meteoritic solar values of Feldman (1992) and where “...” indicates that the abundance of that element is tied to Fe in its meteoritic solar ratio. For models with multiple temperature components the abundances of each component are the same. Finally, the “Constant ξ ” model represents a plasma emitting over a range of temperatures having equal emission measure over equal temperature intervals; for this model T_c represents the temperature of the midpoint of the range while T_h indicates the length of the temperature interval.

To quantify more precisely the evidence for non-isothermal gas we must fit plasma models convolved with the detector response directly to the ASCA spectra. As we have shown in section 2.3 it is vital to consider as many line ratios as possible to distinguish between simple two-temperature and cooling flow models. Hence, in this section we examine mod-

els fitted over 1.6-9 keV which includes the strong Si, S, Ar, Ca, and Fe K shell transitions.

We do not analyze energies below 1.6 keV since the emission near 1 keV is dominated by Fe L emission, and intrinsic absorbing material needs to be considered for lower energies (e.g. Fabian et al. 1994a). The latter point is es-

pecially relevant for our analysis because this allows us to assume (to a good approximation) that the same Galactic column density (Table 6) modifies each spectral component; i.e. this simplification limits the number of free parameters for models that emit over a continuous range of temperatures. We account for absorption by our Galaxy using the photo-electric absorption cross sections according to Balucińska-Church & McCammon (1992).

Since it is our purpose to distinguish between rival spectral models we desire to optimize S/N by rebinning the *ASCA* spectra above the minimum 20 counts (see beginning of section 3.2) so that the energy resolution of the detectors are not greatly over-sampled. For the SIS data we settled on minimums of 50 counts for M87 and 100 counts for Centaurus and Perseus. Since the GIS resolution is poorer than for the SIS we chose larger minimums: 100 counts for M87 and 150 counts for Centaurus and Perseus. The effects of using these larger PI bins are actually small, and the results we present below are consistent with the results obtained from using the standard 20-count binning employed in the previous section.

We again focus on the SIS data to provide a consistent comparison with the results of the previous section, and because they provide the best constraints on the line properties. However, we discuss the additional constraints provided by joint fitting of the SIS and GIS data below in section 3.3.3.

Unlike most previous studies we do not use the photospheric solar abundances of Anders & Grevesse (1989), but instead we use the meteoritic solar abundances of Feldman (1992) which are more appropriate (Ishimaru & Ariimoto 1997). The principal difference is that the meteoritic Fe abundance (Fe/H of 3.24×10^{-5} by number) is 1/1.44 times the photospheric value. Below in section 3.3.2 we discuss how this choice affects our results in comparison to some previous studies.

3.3.1 Constraints on $\xi(T)$

In Table 10 we list the results of fitting isothermal models (1T), two-temperature models (2T), and models with a constant differential emission measure, $\xi(T) = \text{constant}$, to the summed SIS data. The best-fitting 1T and 2T models are displayed at the bottom of Figures 12 - 14. The spike in the residuals of both the 1T and 2T models of Perseus (Figure 14) coincides with the 2.2 keV feature discussed in section 3.2.1. We find that this feature cannot be removed by making simple alterations to $\xi(T)$ which is consistent with the feature being dominated by the systematic error at 2.2 keV arising from the optical constants in the XRT (Gendreau & Yaqoob 1997). Hence, the results listed in Table 10 for Perseus exclude the energies 2-2.8 keV where this feature dominates.

From examination of the residuals in Figures 12 - 14 and the χ^2 null hypothesis probabilities (P) in Table 10 it is clear that 1T models give poor fits ($P \ll 1$) to the SIS spectra of each cluster. The most prominent residuals occur near the Si and Fe lines. We find that P decreases from M87 to Centaurus and then to Perseus which agrees with our conclusion reached in section 3.2.2 using line ratios that an isothermal gas is most strongly excluded for Perseus and

then Centaurus. The 1T models for each cluster require α/Fe ratios different from solar to obtain a best fit.

The 2T models provide superior fits that are formally acceptable ($P > 0.1$) for each cluster. Examination of Figures 12 - 14 reveals no large residuals for these models though some excess emission at higher energies may be indicated which we discuss below in section 3.3.3. Unlike M87 the 2T models of Centaurus and Perseus are not improved significantly when allowing elements different from Fe to be varied separately: the 2T model having the abundances of the elements tied to Fe in their (meteoritic) solar ratios gives $\chi^2/\text{dof}/P$ values of 298.2/304/0.58 and 179.0/168/0.27 respectively for Centaurus and Perseus. (Note S is tied to Fe for Perseus since we exclude the energies 2-2.8 keV from the fits.)

For comparison to the 2T model we examine the simplest model of a gas emitting over a range of temperatures with constant differential emission measure, $\xi(T) = \text{constant}$. This model provides fits that are virtually identical to the 2T models for M87 and Centaurus, and for Perseus the constant- ξ model fits almost as well as the 2T model. Again the fits are not improved significantly for Centaurus and Perseus when allowing multiple abundances to be varied separately: we obtain 310.1/305/0.41 and 195.4/169/0.08 respectively for Centaurus and Perseus for the constant- ξ model where only the total metallicity is varied. We emphasize that these constant- ξ models have qualitatively different emission measure distributions from the 2T models. That is, for lower and upper temperatures denoted by T_{low} and T_{hi} , the constant- ξ models indicate that the hot gas emits at constant emission measure over the following temperature ranges: $T_{\text{low}} \approx 0.92$ keV and $T_{\text{hi}} \approx 3.46$ keV for M87; $T_{\text{low}} \approx 0.92$ keV and $T_{\text{hi}} \approx 5.9$ keV for Centaurus; $T_{\text{low}} \approx 0.43$ keV and $T_{\text{hi}} \approx 9.4$ keV for Perseus.

The strong similarity between the fits of the 2T and constant- ξ models highlights the difficulty in constraining the shape of a general $\xi(T)$ with *ASCA* data. Although we have not presented results for specific multiphase cooling flow models (sections 2.2.3 and 2.3) because of computational expense, the similarity between the fits of the 2T and constant- ξ models is sufficient to demonstrate that multiphase cooling flows also cannot be distinguished from the 2T models; i.e. multiphase cooling flows have σ_ξ intermediate between the 2T and constant- ξ models. Therefore, the fits to the SIS data over 1.6-9 keV for each cluster clearly rule out isothermal gas but cannot determine whether the gas emits at only two temperatures or over a continuous range of temperatures as expected for a multiphase cooling flow.

3.3.2 Abundances

The Fe abundances obtained from isothermal models are very similar to those obtained from the multitemperature models, whereas several of the α/Fe ratios differ from solar for each 1T model but not for the multitemperature models of Centaurus and Perseus. (A possible exception being the sub-solar Ar/Fe ratio for the constant- ξ model of Perseus.) The fact that the Si/Fe ratios exceed solar for 1T models in contrast to the 2T and constant- ξ models is another demonstration of biased measurements of abundances which occur

from fitting a multitemperature spectrum with an isothermal model (e.g. see Appendix of Buote 1999b).

If instead the photospheric solar abundances are used as done in most previous studies, then α/Fe ratios in excess of solar are required to obtain fits of similar quality to the (meteoritic) multitemperature models of Centaurus and Perseus; e.g. using photospheric solar abundances for the 2T model of Centaurus we obtain $Z_{\text{Fe}} = 0.83Z_{\odot}$ $Z_{\text{Si}} = 1.2Z_{\odot}$ $Z_{\text{S}} = 1.1Z_{\odot}$ $Z_{\text{Ar}} = 1.4Z_{\odot}$ $Z_{\text{Ca}} = 1.4Z_{\odot}$. This Si/Fe ratio of $\sim 1.5Z_{\odot}$ (photospheric) is similar to the value of 2 solar (photospheric) obtained by Fukazawa et al. (1998) using isothermal models within an annulus of $0.1h_{50}^{-1} - 0.4h_{50}^{-1}$ Mpc which excludes the region we have analyzed (Table 6). When using the photospheric solar abundances for the 1T model of Centaurus we obtain a Si/Fe ratio of 2 solar in good agreement with Fukazawa et al.. Hence, the Si/Fe enhancements obtained by Fukazawa et al. are due in part to their using photospheric solar abundances, and if the hot gas within their apertures deviates significantly from isothermal then the assumption of isothermal gas contributes as well.

When accounting for the differences between meteoritic and photospheric solar abundances we find that the Fe abundances we have obtained agree well with previous ASCA studies; e.g. for M87 (Matsumoto et al. 1996; Hwang et al. 1997), for Centaurus (Fukazawa et al. 1994; Fabian et al. 1994a), and for Perseus (Fabian et al. 1994a). We mention that for the multitemperature models we do not require the abundances to be different for different temperature components. That is, our models do not require abundance gradients within our apertures but they do not exclude them either. The existence of abundance gradients within our apertures does not compromise the abundances inferred by our simple models because, as we have shown previously for ellipticals and groups (see section 4.1 in Buote 1999b and section 5.3 of Buote 1999a), these models provide accurate measurements of the average Fe abundances obtained from the integrated spectrum within a large spatial region.

3.3.3 Evidence for high energy excesses?

Examination of the residuals from the 2T models (Figures 12 - 14) suggests excess emission for energies above ~ 7 keV for Centaurus and perhaps the other clusters as well. Using simple models we have investigated the contribution of a non-thermal component which manifests itself preferentially at higher energies in the ASCA bandpass. We find that the results for a canonical AGN component (i.e. power law with photon index 1.7 – Mushotzky et al. 1993) are nearly identical to those of a bremsstrahlung component with temperature greater than ~ 10 keV. We shall focus on the results using the AGN model.

In Table 10 we give the results of adding the simple AGN power-law model (PL) to the 1T and 2T models. The 1T models are improved significantly when the PL component is added, but the improvement in each case is not nearly as great as that observed for the 2T models over the 1T models. The PL component only improves the 2T models slightly. A negligible improvement in the multitemperature fits is expected because of the good agreement between the Fe $\text{K}\alpha$ ratios and the local continuum temperatures discussed in section 3.2.2.

It might be expected that when the GIS data are in-

cluded in the fits then, because of its better sensitivity to energies above ~ 8 keV, the need for a power-law component will be made clearer. In fact, we find just the opposite. When the GIS data are included the relative improvement of the 2T+PL model over the 2T models is less for Centaurus and Perseus although for M87 the results are similar to those of the SIS data alone. We find that for the simultaneous SIS+GIS fits for Centaurus and Perseus the SIS residuals exceed the 2T model while the GIS residuals lie below the best-fitting 2T model. Differences between the SIS and GIS at these energies are not unexpected because of the calibration issues mentioned in section 3.2.1 (see Gendreau & Yaqoob 1997). At any rate, the weak evidence for the power-law components obtained from the 2T models (which also applies to constant- ξ models) is unclear because Gendreau & Yaqoob (1997) note that existing calibration errors can give rise to a hard tail in the data. Hence, our spectral analysis does not provide convincing evidence in support of excess hard emission over that produced by the hot plasma components. The lack of excess hard emission in M87 is supported by recent RXTE observations (Reynolds et al. 1999).

We mention as a caveat that if lower energies are included in the fits (e.g. down to ~ 0.6 keV) then the temperatures of the 2T models are lowered (due to the influence of cooler temperature components) and there is more of a need for an additional higher energy component which can be modeled with a (now intrinsically absorbed) power law. However, disentangling the uncertain shape of $\xi(T)$ and the relative contribution of a power-law component from issues of excess absorption and possible uncertainties in the Fe L lines is beyond the scope of this paper; i.e. we conclude that the multitemperature models fitted over 1.6-9 keV, which do not require us to accurately model excess absorption or the Fe L lines, also do not require high energy excesses.

4 PROSPECTS FOR FUTURE MISSIONS

ASCA has provided a tantalizing glimpse of the temperature structure from emission line ratios in a few ellipticals and clusters. We are fortunate that within the next few years satellites will provide superior X-ray data capable of determining $\xi(T)$ with unprecedented precision. Our intention in this section is to give some indication of how well the multi-phase structure of ellipticals and clusters can be probed by these new missions.

We continue with our prototype examples of NGC 4472 and Centaurus to examine how well these new missions can distinguish a cooling flow from a two-temperature plasma (see Section 2.3). That is, we simulate observations of cooling flow models of these clusters (Table 4) and then fit two-temperature models to the simulated data. We then compare ratios of the best-fitting two-temperature models to the simulated data.

4.1 *Chandra* and *XMM*

Our probe into the future begins with the *Chandra X-Ray Observatory*^{††} which is scheduled to launch in 1999 and the

^{††} <http://chandra.harvard.edu>

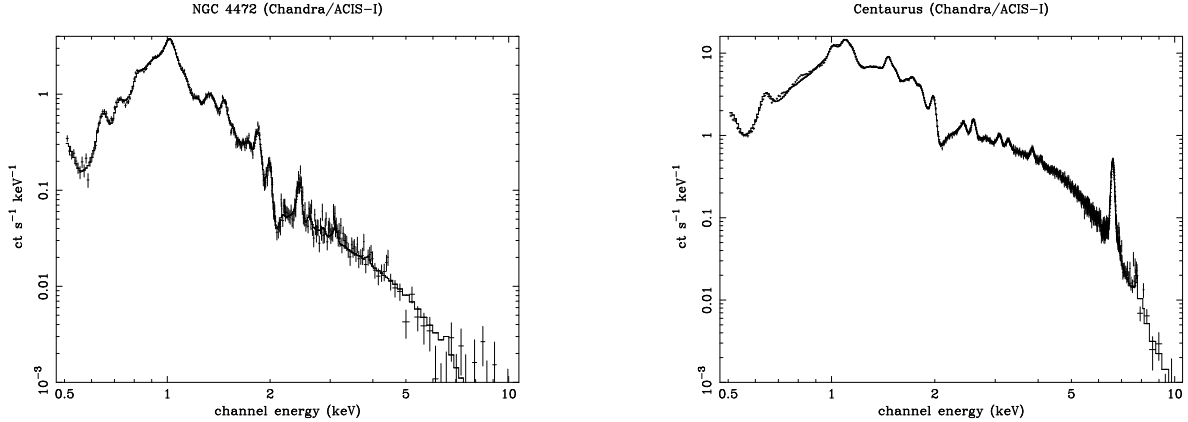


Figure 15. Simulated 100 ks observations of NGC 4472 and Centaurus with the *Chandra* ACIS-I following the cooling flow models in Table 4. The best-fitting two-temperature models are also shown.

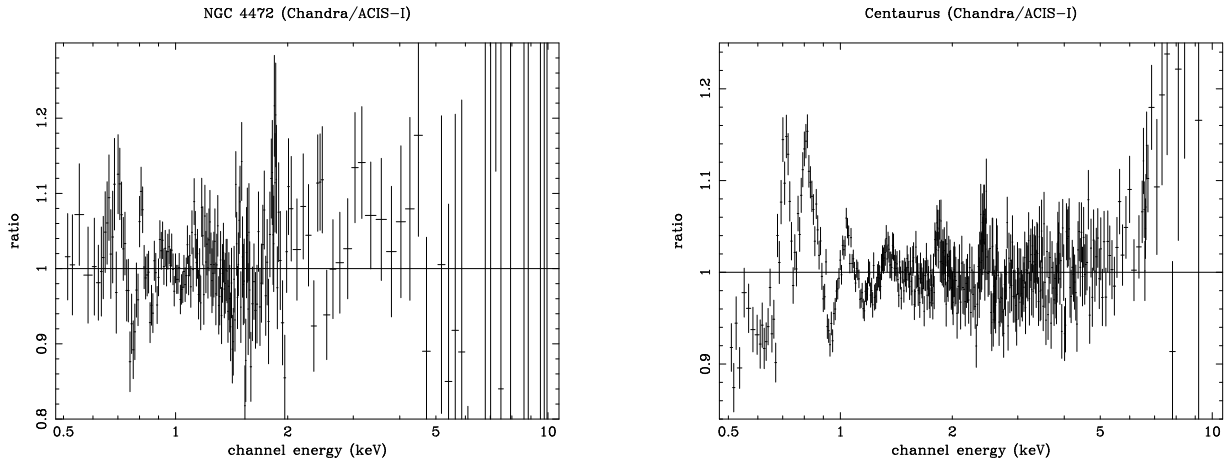


Figure 16. Same as Figure 15 except we plot the ratio of the best-fitting two-temperature model to the simulated data arising from the cooling flow model. Note that we increased the energy bin sizes with respect to Figure 15 for aesthetic reasons.

X-Ray Multi-Mirror Mission (XMM)^{††} which is scheduled to launch in January 2000. The ccds on board these satellites have similar energy resolution, and thus we shall focus on simulations of *Chandra* observations and note any important differences expected from *XMM*.

There are several instruments on board *Chandra*, but we focus our attention on the AXAF CCD Imaging Spectrometer (ACIS) since it is most appropriate for high resolution spectral analysis of extended sources. The energy resolution (and bandwidth) of the four front illuminated CCDs employed in the ACIS imaging array (ACIS-I) is similar to the pre-flight ASCA SIS: e.g. $\Delta E \sim 60$ eV (FWHM) at $E \sim 1$ keV and $\Delta E \sim 140$ eV (FWHM) at $E \sim 6.5$ keV. However, the spatial resolution of the ACIS-I is vastly superior: 90 per cent encircled energy fraction within $1''$ of a 1.5 keV monochromatic point source.

With XSPEC we simulated 100 ks ACIS-I observations of NGC 4472 and Centaurus using the cooling flow models listed in Table 4; we used the default RMF and ARF files supplied for simulating AO1 observations. We included background in these simulations using models for the diffuse

X-ray background and instrumental background following Figure 5.14 of the AXAF Proposers' Guide Rev. 1.0^{§§}. The background-subtracted spectrum of NGC 4472 is shown in Figure 15. Also shown is the best-fitting 2T+Bremsstrahlung (variable N_H for each plasma component, abundances are tied together). In Figure 16 we plot the ratio of the best-fitting 2T+Bremsstrahlung model to the simulated data.

The simulated ACIS-I data for NGC 4472 are of substantially higher quality than the real ASCA data (see Buote 1999a). Line blends of O VIII (H), Mg XI (He) and XII (H), Si XIII (He) and XIV (H), S XV (He) and XVI (He), and Ar XVII (He) are readily apparent. Deviations of the model and simulated data are apparent for the K α lines of Si and S, but the discrepancies are only significant at ~ 90 per cent level. However, the 2T+Bremsstrahlung model is clearly rejected by lines at lower energies. As expected (section 2.3) the most important residuals occur for the Fe L lines from $\sim 0.7 - 0.9$ keV and the O VIII (H1) line.

We note that *XMM* is able to reject the 2T+Bremsstrahlung model with higher confidence than *Chandra*. Firstly, since *XMM* has considerably larger effective area the constraints

^{††} <http://astro.estec.esa.nl/XMM/>

^{§§} <http://asc.harvard.edu/USG/docs/docs.html>

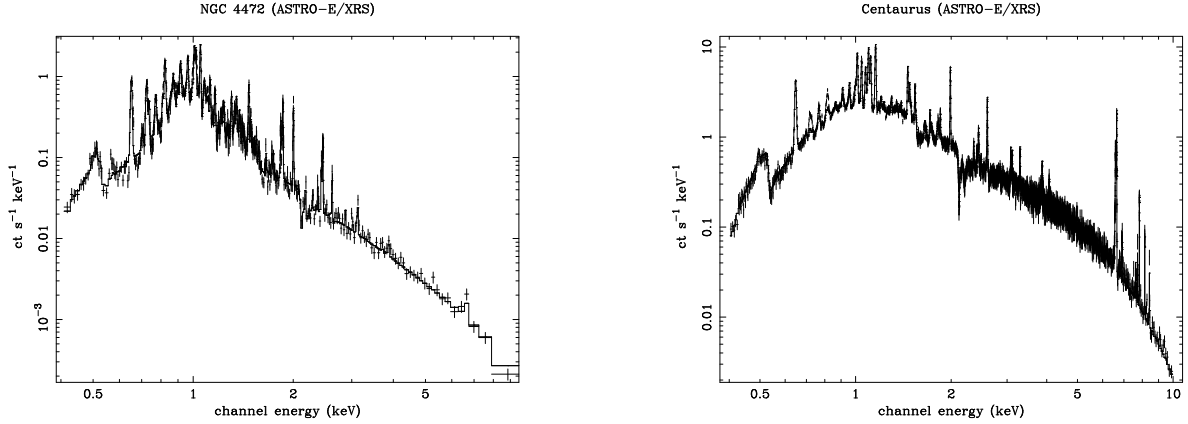


Figure 17. Same as Figure 15 except the observations are simulated for the *ASTRO-E* XRS.

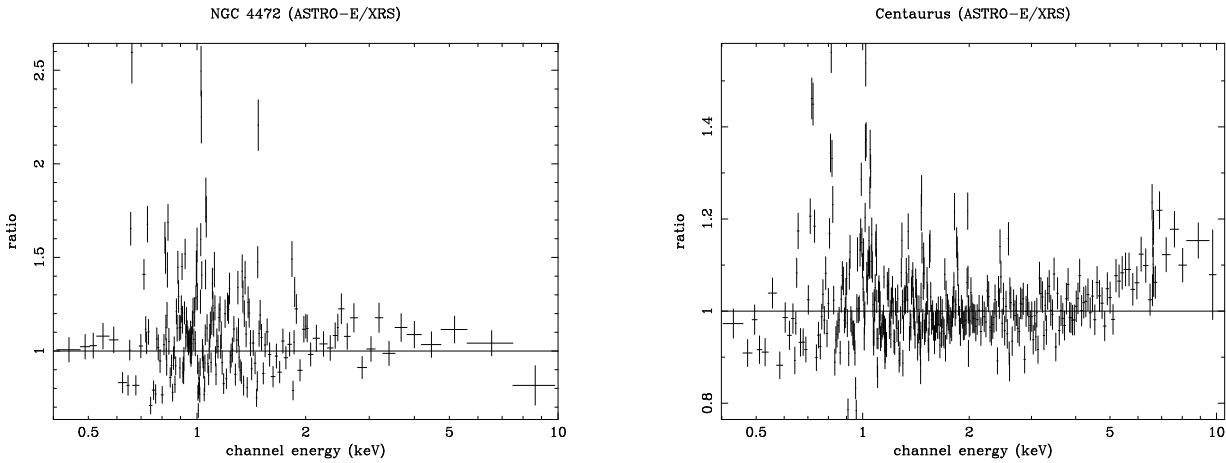


Figure 18. Same as Figure 17 except we plot the ratio of the best-fit two-temperature model to the simulated data arising from the cooling flow model. Note that we increased the energy bin sizes with respect to Figure 17 for aesthetic reasons.

on the $\text{K}\alpha$ lines of Si and S are more precise; i.e. it is not so necessary to appeal to the Fe L lines to reject the two-temperature model. Secondly, the larger bandwidth (0.1-12 keV) of *XMM* makes it more difficult for the two-temperature model to mimic the cooling flow spectrum.

The simulated 100 ks observation of Centaurus and the best-fitting 2T model are also shown in Figure 15; similarly the ratio of the best-fitting 2T model to the simulated data is plotted in Figure 16. All of the line blends detected with the *ASCA* data (Figure 13) are also clearly detected by *Chandra*. Similar to NGC 4472, the line fluxes are better constrained than with *ASCA*. The H/He $\text{K}\alpha$ ratios of Si and S are both marginally inconsistent with the two temperature models at the $\sim 2\sigma$ level as is apparent from the excesses in Figure 16. Again the most substantial deviations of the two-temperature model occur for energies $\lesssim 1$ keV where the Fe L and oxygen lines dominate the spectrum and easily reject the two-temperature fit. Nevertheless, it is significant that the H/He $\text{K}\alpha$ ratios of Si, S, and Fe can independently differentiate the two-temperature and cooling flow models for Centaurus so that issues like the accuracy of the Fe L transitions in the plasma codes and the amount of absorption are not an issue.

4.2 ASTRO-E

After *Chandra* and *XMM* a significant leap forward in energy resolution will be provided by the X-Ray Spectrometer (XRS) on board the *ASTRO-E* satellite^{¶¶} scheduled for launch in March 2000. Unlike previous X-ray detectors, the XRS uses an array of X-ray micro-calorimeters which will provide an unprecedented combination of high energy resolution ($\Delta E \sim 10$ eV FWHM) and large collecting area. Although its spatial resolution is limited and its expected lifetime is only ~ 2 years, the XRS will have the ability to measure individual emission lines of extended sources such as ellipticals, groups, and clusters like no previous X-ray mission.

In analogy to the *Chandra* cases, we simulated 100 ks observations with the XRS for the cooling flow models of NGC 4472 and Centaurus. We used the default RMF, ARF, and background files provided by the *ASTRO-E* GOF web site^{|||}. We show in Figure 17 the simulated XRS spectra and best-fitting two-temperature models of NGC 4472 (2T+BREM) and Centaurus (2T). The ratios of the two-

^{¶¶} <http://lheawww.gsfc.nasa.gov/docs/xray/astroe/>

^{|||} <http://heasarc.gsfc.nasa.gov/docs/astroe/astroegof.html>

temperature models to the simulated data are displayed in Figure 18

With the vastly improved resolution many blends of lines in the *Chandra* and *XMM* (and *ASCA*) data separate. The He-like K α transitions of Si and S become separate He4 lines and blends of He4-5 and satellites; similar transitions of Mg are also resolved. Many new transitions are resolved including the K β lines of Si XIII (He3) and Si XIV (H2). The Fe XXV complex for Centaurus, though still unresolved, shows significant structure indicating separate contributions from the He4, He5-6, and satellites. Large residuals in the two-temperature fits at the energies of these K shell lines shows that finally at the resolution of the XRS the K shell lines can clearly differentiate between two-temperature and cooling flow models for NGC 4472 in addition to Centaurus. The novel constraints on ratios of K β /K α lines of the same element can be used to verify fundamental assumptions of the coronal model; e.g. the assumptions of ionization equilibrium and an optically thin plasma.

Moreover, the oxygen lines and many of the key Fe L blends are easily measured with the XRS. The O VII (He) and OVIII (H1) lines for NGC 4472 clearly distinguish the simulated cooling flow from the two-temperature fit. (Note that allowing the relative abundances of, e.g., O, Ne, Mg, Si, S, Ar, and Ca to be free does not improve the fit substantially.) Of more importance is the Fe XVII blend at ~ 0.7 keV (see Table 3) and other Fe L lines near 1 keV. It is clear that data of this quality will provide exciting new insights into the temperature structure of the hot plasma in these systems.

5 DISCUSSION

5.1 Resonance Scattering

It is usually assumed that the hot gas in ellipticals and clusters is optically thin to X-rays. However, Gil'fanov, Syunyaev, & Churazov (1987) have argued that resonance scattering of photons produced by strong transitions to the ground state of an abundant ion may be important in these systems. Gil'fanov et al. estimated significant optical depths $\tau \sim 4.0$ and 2.7 to the Fe XXV (He4) line in the centers of Perseus and M87 respectively. They predicted that steeply rising abundance profiles with increasing radius should be observed if the intrinsic abundances are constant with radius.

In fact, observations of clusters almost always show flat abundance profiles or, particularly for cooling flow clusters, abundance profiles that increase towards the center (e.g. Fukazawa et al. 1994). It would seem unlikely that in most cases the nearly flat abundance profiles of observed clusters are actually due to large intrinsic negative abundance gradients which almost exactly cancel the predicted effect due to resonance scattering. As noted by Gil'fanov et al., turbulent motions in the gas may significantly reduce the importance of resonance scattering. (Turbulent velocities of ~ 300 km s $^{-1}$ should be sufficient to reduce the optical depth of the Fe XXV He4 line below unity in a massive cluster.) Fortunately, as shown by Gil'fanov et al., resonance scattering modifies the observed line shapes and thus its importance may be directly measured by future missions with sufficient energy resolution (e.g. *Constellation-X*).

As shown in section 3.2.2 the Fe K β /K α ratio measured from the *ASCA* data of Perseus is consistent with optically thin plasma and does not suggest resonance scattering in contrast to the result obtained by Molendi et al. (1998) using *SAX* data. Although resolving the discrepancy between the *ASCA* and *SAX* results is beyond the scope of our paper, we believe the consistent results we have obtained for M87, Centaurus, and Perseus using *ASCA* data argue that resonance scattering has a negligible impact on the Fe abundances inferred from current X-ray data.

5.2 Multiphase Strengths of Clusters and Ω_0

Since structure formation in the Universe is believed to proceed by hierarchical clustering, galaxy clusters should show evidence of merging depending on their dynamical “age”. The relative fraction of dynamically young clusters in a complete cluster sample should be sensitive to the cosmological density parameter Ω_0 as first suggested by Richstone, Loeb, & Turner (1992). Recent analysis of X-ray cluster morphologies favors a universe with low matter density $\Omega_0 \sim 0.35$ (Buote & Xu 1997).

Cluster morphologies, however, are only one indicator of the dynamical states of clusters. The dynamical state indicated by cluster morphology is the same as that indicated by the quantity, $\Delta M/\bar{M}$, the fractional amount of mass a cluster accreted during the previous crossing time, but the connection between cluster morphology and $\Delta M/\bar{M}$ (and thus Ω_0) is rigorously valid only for clusters that are not very close to a virialized state (see section 2.1 of Buote 1998).

In contrast, the temperature structure of clusters can provide a sensitive measure of the dynamical states of nearly relaxed clusters. For illustrative purposes, let us consider a massive cluster ($T \sim 8$ keV) which has recently formed. At this time there will be little or no contribution to the emission measure ($\xi(T)dT$) from a cooling flow since arguments (McGlynn & Fabian 1984) and *ROSAT* data (Buote & Tsai 1996; see also Jones & Forman 1999) show that the presence of cooling flows anti-correlates with substantial substructure. Within the central few hundred kpc there will be significant temperature fluctuations arising from incomplete relaxation (e.g. as in A754 and A2256 – Henry & Briel 1995 and Briel & Henry 1995). When the cluster has relaxed to a state that is close to the onset of a cooling flow, the emission measure distribution will be peaked near $T \sim 8$ keV along with residual temperature fluctuations. In terms of the multiphase strength (Section 2.2.1), such a cluster about to start a cooling flow will have typically $\sigma_\xi \lesssim 0.1$.

As the cluster relaxes a cooling flow will gradually develop. The emission measure distribution will widen until it resembles those in Figure 9 with $\sigma_\xi \sim 0.7$ - 0.8. (Within the central few hundred kpc the cooling flow can contribute up to ~ 80 - 90 per cent of the X-ray emission; e.g. Fabian 1994.) Notice that the dynamic range in σ_ξ between a cooling flow cluster (~ 0.7) and an incipient cooling flow ($\lesssim 0.1$) is considerably larger than the difference between an incipient cooling flow and an isothermal gas ($\sigma_\xi = 0$); i.e. the temperature structure, expressed in terms of σ_ξ , is a sensitive discriminant of the “age” of nearly relaxed clusters unlike cluster morphologies.

However, clusters which have recently experienced major mergers can have a wide distribution of temperature

components contributing to the emission measure, which in some cases may give σ_ξ comparable to cooling-flow clusters. It will be necessary, as a result, to consider the joint σ_ξ and morphology (e.g. $\log_{10} P_m/P_0$ – Buote & Tsai 1995) distributions to remove this potential degeneracy of cluster ages with large σ_ξ . Hence, with future X-ray satellites capable of detailed mapping of the emission measure distributions of clusters (e.g. *ASTRO-E*, *Constellation-X*), the multiphase strength σ_ξ can be measured for many clusters and be compared to those produced in N-body/ Hydrodynamical simulations (and combined with information from cluster morphologies) in order to constrain Ω_0 .

It is possible with currently available data from *ASCA* to estimate σ_ξ of many clusters without detailed mapping of $\xi(T)$ for each cluster. This is possible if one assumes that the true $\xi(T)$ of clusters is accurately represented by a two component model consisting of a constant pressure cooling flow and an isothermal ambient gas component (e.g. cooling flow models in Table 4). As described in section 2.2.1, the multiphase strength of such models is just $f\sigma_\xi$, where σ_ξ is the multiphase strength of the cooling flow component (Figure 8) and f is the fractional contribution of the cooling flow to the total emission measure. Since these two-component models describe the available data of clusters quite well, this procedure for estimating σ_ξ should be a good approximation in most cases.

6 CONCLUSIONS

We have studied the ability of X-ray emission line ratios to probe the temperature structure of elliptical galaxies and galaxy clusters using theoretical models, the best available *ASCA* data, and simulated observations with *Chandra* and *ASTRO-E*. We have emphasized multiphase spectra consisting of either two temperatures or cooling flow models and examined the best means of distinguishing between them. Ratios of lines of K shell transitions have been emphasized over the Fe L lines because of possible remaining inaccuracies in the available plasma codes.

From analysis of isothermal MEKAL models computed with energy resolution 2 eV (FWHM) appropriate for the proposed *Constellation-X* mission, we found that the most useful ratios of K shell transitions for probing the emission measure distributions of ellipticals and clusters are the H1/He4 ($K\alpha$) and satellite/He4 ratios of the same element (notation described in Table 1). The H2/H1 and He3/He4 ratios ($K\beta/K\alpha$) are much less temperature sensitive for temperatures where the transitions are strong. Ratios of similar transitions of different elements (e.g., He4 of S/Fe) are very temperature sensitive but must be used with caution for interpreting temperatures structure since they depend on the relative abundances of the elements. Finally, we also discuss the very strong temperature dependence of a few ratios of Fe L lines between ~ 0.7 - 1.4 keV which are typically the strongest lines and most temperature sensitive ratios of all.

We considered a few simple multiphase models to evaluate how well the various line ratios can constrain the general differential emission measure $\xi(T)$. To facilitate quantitative comparison of ellipticals and clusters having different $\xi(T)$ we introduced the “multiphase strength” parameter, σ_ξ , which measures the fractional width of $\xi(T)$: $\sigma_\xi = 0$

for an isothermal gas and $\sigma_\xi \cong 1$ for a constant emission measure distributed over a large temperature range. Of the simple multiphase models examined (two temperature, constant emission measure, gaussian emission measure, cooling flows) it is found that the two-temperature models have the most flexibility; i.e. for a given value of $\langle T \rangle$ (emission measure weighted temperature) the two-temperature models can generally provide the best approximation to a given line ratio.

The flexibility of the two-temperature model is illustrated by its ability to match very closely a model consisting of a cooling flow component and a single temperature component corresponding to ambient gas (Figure 10). Cooling flows have nearly maximal multiphase strength ($\sigma_\xi \sim 0.7$), but their $K\alpha$ line ratios (aside from O) can be approximated by two temperature models within ~ 20 per cent for elliptical galaxies like NGC 4472 and within ~ 50 per cent for clusters like Centaurus. The best means to distinguish between two-temperature models and cooling flows is to use oxygen lines or Fe L lines whose ratios can differ by a factor of ~ 10 between the models.

We have re-analyzed the *ASCA* spectra of three of the brightest galaxy clusters to assess the evidence for multiphase gas in their cores: M87 (Virgo), the Centaurus cluster, and the Perseus cluster. $K\alpha$ emission line blends of Si, S, Ar, Ca, and Fe are detected in each system as is significant Fe $K\beta$ emission. The Fe $K\beta/K\alpha$ ratios are consistent with optically thin plasma models and do not suggest resonance scattering in these systems. Consideration of both the ratios of H-like to He-like $K\alpha$ lines and the continuum temperatures clearly rules out isothermal gas in each case.

To obtain more detailed constraints we fitted plasma models over 1.6-9 keV where the emission is dominated by these K shell lines and by continuum. In each case the *ASCA* spectra cannot determine whether the gas emits at only two temperatures or over a continuous range of temperatures as expected for a cooling flow. The metal abundances are near solar for all of the multiphase models. For Centaurus and Perseus the Si/Fe ratios are consistent with the meteoritic solar values. We also find that our multitemperature models fitted over 1.6-9 keV, which do not require us to accurately model excess absorption or the Fe L lines, also do not require any excess emission at higher energies from, e.g, an AGN component.

We examined the ability of future X-ray missions to constrain $\xi(T)$ in ellipticals and clusters. By simulating observations with the *Chandra* ACIS-I and the *ASTRO-E* XRS of cooling flow models of NGC 4472 and Centaurus we found that these future instruments will have the ability to distinguish between two-temperature models and cooling flows. However, the lower resolution *Chandra* ACIS-I (and also the *XMM* ccds) must rely on constraints from O and Fe L lines for definitive results whereas the *ASTRO-E* XRS only requires the $K\alpha$ lines above ~ 2 keV (e.g. Si and S).

We have discussed the evidence for resonance scattering in light of our results for the $K\beta/K\alpha$ ratios. We also discuss the multiphase strength, σ_ξ , as an indicator of the dynamical states of clusters and its potential use as a probe of Ω_0 in conjunction with galaxy cluster morphologies.

The difficulty in distinguishing between different multiphase models, specifically a two-temperature plasma from a cooling flow, has been emphasized in this paper. Presently,

there are only a few cases where line ratios have been measured with sufficient precision to merely indicate that the gas is not isothermal. It is imperative that the temperature structures of ellipticals and clusters be considered when interpreting properties (e.g. abundances) derived from spectral fits in these systems.

ACKNOWLEDGMENTS

We thank J. Kaastra and the referee, M. Loewenstein, for helpful comments. This research has made use of ASCA data obtained from the High Energy Astrophysics Science Archive Research Center (HEASARC), provided by NASA's Goddard Space Flight Center. DAB acknowledges support for this work provided by NASA through Chandra Fellowship grant PF8-10001 awarded by the Chandra Science Center, which is operated by the Smithsonian Astrophysical Observatory for NASA under contract NAS8-39073.

REFERENCES

Anders E., Grevesse N., 1989, *Geochimica et Cosmochimica Acta*, 53, 197

Arnaud K., 1996, in Jacoby G. and Barnes J., eds., *Astronomical Data Analysis Software and Systems V*, ASP Conf. Series volume 101, p17

Bahcall J. N., Sarazin C. L., 1977, *ApJ*, 219, 781

Balucińska-Church M., McCammon D., 1992, 400, 699

Boehringer H., Tanaka Y., Mushotzky R. F., Ikebe Y., Hattori M., 1998, *A&A*, 334, 789

Briel U. G., Henry J. P., 1995, *Nature*, 372, 439

Brightenti F., Mathews W. G., 1999b, *ApJ*, in press (astro-ph/9811258)

Buote D. A., 1998, *MNRAS*, 293, 381

Buote D. A., 1999a, *MNRAS*, in press (astro-ph/9811080)

Buote D. A., 1999b, *MNRAS*, submitted (astro-ph/9903278)

Buote D. A., Canizares C. R., 1998, *MNRAS*, 298, 811

Buote D. A., Fabian A. C., 1998, *MNRAS*, 296, 977

Buote D. A., Tsai J. C., 1995, *ApJ*, 452, 522

Buote D. A., Tsai J. C., 1996, *ApJ*, 458, 27

Buote D. A., Xu G., 1997, *MNRAS*, 284, 439

Canizares C. R., Clark G. W., Jernigan J. G., Markert T. H., 1982, *ApJ*, 262, 33

Canizares C. R., Markert T. H., Donahue M. E., 1988, in Fabian A. C., ed., *Cooling Flows in Clusters of Galaxies*, (Kluwer: Dordrecht), 63

Ciotti L., D'Ercole A., Pellegrini S., Renzini A., 1991, *ApJ*, 376, 380

Craig I. J. D., Brown J. C., 1976, *A&A*, 49, 239

David L. P., Jones C., Forman W., 1991, *ApJ*, 380, 39

David L. P., Jones C., Forman W., Daines S., 1994, *ApJ*, 428, 544

Dickey J. M., Lockman F. J., 1990, *ARA&A*, 28, 215

Dotani, et al., Recent Progress of SIS Calibration and Software, in *ASCA News #5* (NASA/GSFC: Greenbelt), 14

Fabian A. C., 1994, *ARA&A*, 32, 277

Fabian A. C., Nulsen P. E. J., Canizares C. R., 1984, *Nature*, 310, 733

Fabian A. C., Arnaud K. A., Bautz M. W., Tawara Y., 1994a, *ApJ*, 436, L63

Fabian A. C., Crawford C. S., Edge A. C., Mushotzky R. F., 1994b, *MNRAS*, 267, 779

Feldman U., 1992, *Physica Scripta*, 46, 202

Forman W., Jones C., David L., Franx M., Makishima K., Ohashi T., 1993, *ApJ*, 418, L55

Fukazawa Y., Ohashi T., Fabian A. C., Canizares C. R., Ikebe Y., Makishima K., Mushotzky R. F., Yamashita K., 1994, *PASJ*, 46, L55

Fukazawa Y., et al., 1998, *PASJ*, 50, 187

Gendreau K., Yaqoob T., 1997, *ASCA XRT Calibration Issues*, in *ASCA News vol. 5*, (NASA/GSFC: Greenbelt), 8

Gil'fanov M. R., Syunyaev R. A., Churazov E. M., 1987, *Sov. Astron. Lett.*, 13, 3

Henry J. P., Briel U. G., 1995, *ApJ*, 443, L9

Hwang U., Mushotzky R. F., Loewenstein M., Markert T. H., Fukazawa Y., Matsumoto H., 1997, *ApJ*, 476, 560

Irwin J. A., Sarazin C. L., 1996, *ApJ*, 471, 683

Ishimaru Y., Arimoto N., 1997, *PASJ*, 49, 1

Johnstone R. M., Fabian A. C., Edge A. C., Thomas P. A., 1992, *MNRAS*, 255, 431

Jones C., Forman W., 1999, *ApJ*, 511, 65

Jones C., Stern C., Forman W., Breen J., David L., Tucker W., Franx M., 1997, *ApJ*, 482, 143

Judge P. G., Hubeny V., Brown J. C., 1997, *ApJ*, 475, 275

Kaastra J. S., Mewe R., 1993, *A&AS*, 97, 443

Kaastra J. S., Mewe R., Liedahl D. A., Singh K. P., White N. E., Drake S. A., 1996, *A&A*, 314, 547

Kunieda H., et al., XRT Status Report, in *ASCA News vol. 5*, (NASA/GSFC: Greenbelt), 3

Liedahl D. A., Osterheld A. L., Goldstein W. H., 1995, *ApJ*, 438, L115

Loewenstein M., Mathews W. G., 1991, *ApJ*, 373, 445

Loewenstein M., Mushotzky R. F., 1996, *ApJ*, 466, 695

Matsumoto H., Koyama K., Awaki H., Mushotzky R. F., Hatsukade I., 1996, *PASJ*, 48, 201

McGlynn T. A., Fabian A. C., 1984, *MNRAS*, 208, 709

Mewe R., 1991, *A&ARev*, 3, 127

Mewe R., Gronenschild E. H. B. M., van den Oord G. H. J., 1985, *A&AS*, 62, 197

Molendi S., Matt G., Antonelli L. A., Fiore F., Fusco-Femiano R., Kaastra J., C. Maccarone, Perola C., 1998, *ApJ*, 499, 608

Mushotzky R. F., Done C., Pounds K. A., 1993, *ARA&A*, 31, 717

Nulsen P. E. J., 1986, *MNRAS*, 221, 377

Nulsen P. E. J., 1997, in Soker N. ed., *Galactic and Cluster Cooling Flows*, ASP Conf. Series, Vol. 115, (ASP: San Francisco), 135

Nulsen P. E. J., 1998, *MNRAS*, 297, 1109

Parmar A., et al., 1997, *A&AS*, 122, 309

Pellegrini S., 1999, *A&A*, 343, 23

Peres C. B., Fabian A. C., Edge A. C., Allen S. W., Johnstone R. M., White D. A., 1998, *MNRAS*, 298, 416

Rangarajan F. V. N., Fabian A. C., Forman W. R., Jones C., 1995, *MNRAS*, 272, 665

Renzini A., 1997, *ApJ*, 488, 35

Reynolds C. S., Heinz S., Fabian A. C., Begelman M. C., 1999, *ApJ*, in press (astro-ph/9812031)

Richstone D. O., Loeb A., Turner E. L., 1992, *ApJ*, 393, 477

Sarazin C. L., 1986, *Rev. Mod. Phys.*, 58, 1

Sarazin C. L., Bahcall J. N., 1977, *ApJS*, 34, 451

Savin D. W., 1999, *ApJ*, in press (astro-ph/9904258)

Savin D. W., et al., 1999, *ApJS*, in press (astro-ph/9903203)

Schmitt J. H. M. M., Drake J. J., Stern R. A., Haisch B., 1996, *ApJ*, 457, 882

Stewart G., Canizares C. R., Fabian A. C., Nulsen P. E. J., 1984, *ApJ*, 278, 536

Tanaka Y., Inoue H., & Holt S. S., 1994, *PASJ*, 46, L37

Thomas P. A., Fabian A. C., Nulsen P. E. J., 1987, *MNRAS*, 228, 973

Trinchieri G., Kim D.-W., Fabbiano G., Canizares C., 1994, *ApJ*, 428, 555

Trümper J., 1983, *Adv. Space Res.*, 2, 241

White R. E. III, Sarazin C. L., 1987, *ApJ*, 318, 621

Wise M. W., Sarazin C. L., 1993, *ApJ*, 415, 58